Mon. Not. R. Astron. Soc. **364,** 753–772 (2005) doi:10.1111/j.1365-2966.2005.09630.x

Turbulent gas motions in galaxy cluster simulations: the role of smoothed particle hydrodynamics viscosity

K. Dolag,[1,2⋆] F. Vazza,[1] G. Brunetti[3] and G. Tormen[1]

[1]*Dipartimento di Astronomia, Universita di Padova, vicolo dell'Osservatorio 2, 35122 Padova, Italy*
[2]*Max-Planck-Institut für Astrophysik, Garching, Germany*
[3]*INAF, Istituto di Radioastronomia, via P.Gobetti 101, 40129 Bologna, Italy*

Accepted 2005 September 19. Received 2005 September 9; in original form 2005 July 21

ABSTRACT

Smoothed particle hydrodynamics (SPH) employs an artificial viscosity to properly capture hydrodynamic shock waves. In its original formulation, the resulting numerical viscosity is large enough to suppress structure in the velocity field on scales well above the nominal resolution limit, and to damp the generation of turbulence by fluid instabilities. This could artificially suppress random gas motions in the intracluster medium (ICM), which are driven by infalling structures during the hierarchical structure formation process. We show that this is indeed the case by analysing results obtained with an SPH formulation where an individual, time-variable viscosity is used for each particle, following a suggestion by Morris & Monaghan. Using test calculations involving strong shocks, we demonstrate that this scheme captures shocks as well as the original formulation of SPH, but, in regions away from shocks, the numerical viscosity is much smaller. In a set of nine high-resolution simulations of cosmological galaxy cluster formation, we find that this low-viscosity formulation of SPH produces substantially higher levels of turbulent gas motions in the ICM, reaching a kinetic energy content in random gas motions (measured within a 1-Mpc cube) of up to 5–30 per cent of the thermal energy content, depending on cluster mass. This also has significant effects on radial gas profiles and bulk cluster properties. We find a central flattening of the entropy profile and a reduction of the central gas density in the low-viscosity scheme. As a consequence, the bolometric X-ray luminosity is decreased by about a factor of 2. However, the cluster temperature profile remains essentially unchanged. Interestingly, this tends to reduce the differences seen in SPH and adaptive mesh refinement simulations of cluster formation. Finally, invoking a model for particle acceleration by magnetohydrodynamics waves driven by turbulence, we find that efficient electron acceleration and thus diffuse radio emission can be powered in the clusters simulated with the low-viscosity scheme provided that more than 5–10 per cent of the turbulent energy density is associated with fast magneto-sonic modes.

Key words: hydrodynamics – turbulence – methods: numerical – galaxies: clusters: general.

1 INTRODUCTION

In hierarchical cold dark matter (CDM) cosmologies, large structures form through the accretion of smaller structures (e.g. White, Briel & Henry 1993). In particular, mergers and infall of haloes play a fundamental role in determining the structure and dynamics of massive clusters of galaxies, where mergers can induce large-scale bulk motions with velocities of the order of $\sim$1000 km s^{-1} or larger. This results in complex hydrodynamic flows where most of the kinetic energy is quickly dissipated to heat by shocks, but some part may in principle also excite long-lasting turbulent gas motions.

Numerical simulations of merging clusters (e.g. Schindler & Mueller 1993; Roettiger, Loken & Burns 1997; Ricker & Sarazin 2001; Takizawa 2005) provide a detailed description of the gas-dynamics during a merger event. It has been shown that infalling subclusters can generate laminar bulk flows through the primary cluster and inject turbulent eddies via Kelvin–Helmholtz (KH) instabilities at interfaces between the bulk flows and the primary cluster gas. Such eddies redistribute the energy of the merger through the cluster volume in a few turnover times, which corresponds to a time interval of the order of 1 Gyr. The largest eddies decay with time into more random and turbulent velocity fields, eventually developing

⋆E-mail: kdolag@mpa-garching.mpg.de

© 2005 The Authors. Journal compilation © 2005 RAS

a turbulent cascade with a spectrum of fluctuations expected to be close to a Kolmogorov spectrum.

Observationally, spatially resolved gas pressure maps of the Coma cluster obtained from a mosaic of *XMM–Newton* observations have indeed revealed the signature of mildly supersonic turbulence, at least in the central regions of the cluster (Schuecker et al. 2004). It has also been suggested that the microcalorimeters on board future X-ray satellites such as *ASTRO-E2* should be able to detect the turbulent broadening of the lines of heavy ions in excess of the thermal broadening (Inogamov & Sunyaev 2003), which would represent a direct measurement of cluster turbulence. Unfortunately, recently it turned out that the main instrument on board the successfully launched *ASTRO-E2* satellite has serious problems; therefore we will have to wait for future missions with similar high-energy resolution to further address these questions observationally.

Cluster turbulence could in principle store an appreciable fraction of the thermal energy of massive clusters, which would make it an important factor for understanding the structure of the intracluster medium (ICM). Shear flows associated with cluster turbulence and the resulting dynamo processes could considerably amplify the magnetic field strength in the ICM (e.g. Dolag, Bartelmann & Lesch 1999, 2002). In addition, magnetohydrodynamics (MHD) waves can be efficiently injected in the ICM directly by shocks, by KH or Rayleigh–Taylor instabilities, or by the decay of turbulent eddies at larger scales. These waves, as well as shocks, can efficiently accelerate supra-thermal particles in the ICM to higher energies. Although there is still some debate concerning the detailed mechanism responsible for the origin of relativistic particles and magnetic fields in the ICM (e.g. Brunetti 2003), the presence of relativistic electrons and of $\sim \mu$G-strength magnetic fields in the ICM is proven by non-thermal emission studied with radio observations and possibly observations of hard X-ray emission (see, for example, Feretti, Gioia & Giovannini 2002; Fusco-Femiano et al. 2003, for a review). In addition, the occurrence of non-thermal phenomena is found to be related to the dynamical state and mass of the parent cluster (Giovannini, Tordi & Feretti 1999; Buote 2001; Schuecker et al. 2001; Feretti 2002), which suggests a connection between cluster mergers and non-thermal activity.

Despite this potentially significant relevance of turbulence for the ICM, quantitative studies have received comparatively little attention in hydrodynamic cluster simulations thus far. One reason for this is that three-dimensional (3D) turbulence is difficult to resolve in any numerical scheme, because these always introduce some finite numerical viscosity, effectively putting a limit on the Reynolds numbers that can still be adequately represented. In the Lagrangian smoothed particle hydrodynamics (SPH) method, which has been widely employed for studies of cluster formation, an artificial viscosity is used to capture shocks. The original parametrization of this viscosity (Monaghan & Gingold 1983) makes the scheme comparatively viscous; it smoothes out small-scale velocity fluctuations and viscously damps random gas motions well above the nominal resolution limit. This hampers the ability of the original SPH to develop fluid turbulence down to the smallest resolved scales.

However, the numerical viscosity of SPH can in principle be reduced by using a more sophisticated parametrization of the artificial viscosity. Ideally, the viscosity should only be present in a hydrodynamic shock, but otherwise it should be negligibly small. To come closer to this goal, Morris & Monaghan (1997) proposed a numerical scheme where the artificial viscosity is treated as an independent dynamical variable for each particle, with a source term triggered by shocks, and an evolutionary term that lets the viscosity decay in regions away from shocks. In this way, one can hope that shocks can still be captured properly, while in the bulk of the volume of a simulation, the effective viscosity is lower than in original SPH. We adopt this scheme and implement it in a cosmological simulation code. We then apply it to high-resolution simulations of galaxy cluster formation, allowing us to examine a better representation of turbulent gas motions in SPH simulations of clusters. This also shines new light on differences in the results of cosmological simulations between different numerical techniques.

In Section 2, we discuss different ways of implementing the artificial viscosity in SPH. We demonstrate in Section 3 the robustness of our new low-viscosity scheme by applying it to several test problems. In Sections 4, 5 and 6, we introduce our set of cluster simulations, the algorithm to detect and measure turbulence, and the implications of the presence of turbulence for the structure and properties of galaxy clusters. In Section 7, we consider the effects of turbulence on the linewidth of narrow X-ray metal lines. Finally, in Section 8 we apply the results from our new simulations to models for the production of radio emission due to turbulent acceleration processes. We give our conclusions in Section 9.

2 SIMULATION METHOD

The SPH method treats shocks with an artificial viscosity, which leads to a broadening of shocks and a relatively rapid vorticity decay. To overcome these problems, Morris & Monaghan (1997) proposed a new parametrization of the artificial viscosity capable of reducing the viscosity in regions away from shocks, where it is not needed, while still being able to capture strong shocks reliably. We have implemented this method in the cosmological SPH code GADGET-2 (Springel 2005), and we describe the relevant details in the following.

In GADGET-2, the viscous force is implemented as

$$\frac{\mathrm{d}v_i}{\mathrm{d}t} = -\sum_{j=1}^{N} m_j \Pi_{ij} \nabla_i \bar{W}_{ij}, \tag{1}$$

and the rate of entropy change due to viscosity is

$$\frac{\mathrm{d}A_i}{\mathrm{d}t} = \frac{1}{2}\frac{\gamma-1}{\rho_i^{\gamma-1}} \sum_{j=1}^{N} m_j \Pi_{ij} \boldsymbol{v}_{ij} \cdot \nabla_i \bar{W}_{ij}, \tag{2}$$

where $A_i = (\gamma - 1)u_i/\rho_i^{\gamma-1}$ is the entropic function of a particle of density ρ_i and thermal energy u_i per unit mass, and $\bar{W}_{ij}$ denotes the arithmetic mean of the two kernels $W_{ij}(h_i)$ and $W_{ij}(h_j)$. The usual parametrization of the artificial viscosity (Monaghan & Gingold 1983; Balsara 1995) for an interaction of two particles i and j includes terms to mimic a shear and bulk viscosity. For standard cosmological SPH simulations, it can be written as

$$\Pi_{ij} = \frac{-\alpha c_{ij}\mu_{ij} + \beta\mu_{ij}^2}{\rho_{ij}} f_{ij}, \tag{3}$$

for $\boldsymbol{r}_{ij} \cdot \boldsymbol{v}_{ij} \leqslant 0$ and $\Pi_{ij} = 0$ otherwise, i.e. the pair-wise viscosity is only non-zero if the particle are approaching each other. Here

$$\mu_{ij} = \frac{h_{ij}\boldsymbol{v}_{ij} \cdot \boldsymbol{r}_{ij}}{\boldsymbol{r}_{ij}^2 + \eta^2}, \tag{4}$$

c_{ij} is the arithmetic mean of the two sound speeds, ρ_{ij} is the average of the densities, h_{ij} is the arithmetic mean of the smoothing lengths, and $\boldsymbol{r}_{ij} = \boldsymbol{r}_i - \boldsymbol{r}_j$ and $\boldsymbol{v}_{ij} = \boldsymbol{v}_i - \boldsymbol{v}_j$ are the interparticle distance and relative velocity, respectively. We have also included a viscosity limiter $f_{ij} = (f_i + f_j)/2$, which is often used to suppress the viscosity

locally in regions of strong shear flows, as measured by

$$f_i = \frac{|\langle \nabla \cdot \boldsymbol{v} \rangle_i|}{|\langle \nabla \cdot \boldsymbol{v} \rangle_i| + |\langle \nabla \times \boldsymbol{v} \rangle_i| + \sigma_i}, \tag{5}$$

which can help to avoid spurious angular momentum and vorticity transport in gas disks (Steinmetz 1996). Note however that the parameters describing the viscosity (with common choices $\alpha = 0.75$–1.0, $\beta = 2\alpha$, $\eta = 0.01 h_{ij}$ and $\sigma_i = 0.0001 c_i/h_i$) remain here fixed in time. This then defines the 'original' viscosity scheme usually employed in cosmological SPH simulations. We refer to runs performed with this viscosity scheme as 'ovisc' simulations.

As a variant of the original parametrization of the artificial viscosity, GADGET-2 can use a formulation proposed by Monaghan (1997) based on an analogy with Riemann solutions of compressible gas dynamics. In this case, μ_{ab} is defined as

$$\mu_{ij} = \frac{\boldsymbol{v}_{ij} \cdot \boldsymbol{r}_{ij}}{|\boldsymbol{r}_{ij}|}, \tag{6}$$

and one introduces a signal velocity $v_{ij}^{\rm sig}$, for example in the form

$$v_{ij}^{\rm sig} = c_i + c_j - 3\mu_{ij}. \tag{7}$$

The resulting viscosity term then changes into

$$\Pi_{ij} = \frac{-0.5\alpha v_{ij}^{\rm sig} \mu_{ij}}{\rho_{ij}} f_{ij}. \tag{8}$$

We have also performed simulations using this signal velocity based artificial viscosity and found that it performs well in all test problems we have examined so far, while in some cases it performed slightly better, in particular avoiding post-shock oscillations in a more robust way. We refer to simulations performed using this 'signal velocity' based viscosity scheme as 'svisc' simulations.

The idea proposed by Morris & Monaghan (1997) is to give every particle its own viscosity parameter α_i, which is allowed to evolve with time according to

$$\frac{{\rm d}\alpha_i}{{\rm d}t} = -\frac{\alpha_i - \alpha_{\rm min}}{\tau} + S_i. \tag{9}$$

This causes α_i to decay to a minimum value $\alpha_{\rm min}$ with an e-folding time τ, while the source term S_i is meant to make α_i rapidly grow when a particle approaches a shock. For the decay time-scale, Morris & Monaghan (1997) proposed to use

$$\tau = h_i/(c_i\, l), \tag{10}$$

where h_i is the smoothing length, c_i is the sound speed and l is a free (dimensionless) parameter which determines on how many information crossing times the viscosity decays. For an ideal gas and a strong shock, this time-scale can be related to a length-scale $\delta = 0.447/l$ (in units of the smoothing length h_i) on which the viscosity parameter decays behind the shock front. For the source term S_i, we follow Morris & Monaghan (1997) and adopt

$$S_i = S^* f_i \max(0, -|\langle \nabla \cdot \boldsymbol{v} \rangle_i|), \tag{11}$$

where $\langle \nabla \cdot \boldsymbol{v} \rangle_i$ denotes the usual SPH estimate of the divergence around the particle i. Note that it would in principle be possible to use more sophisticated shock detection schemes here, but the simple criterion based on the convergence of the flow is already working well in most cases. We refer to simulations carried out with this 'low'-viscosity scheme as 'lvisc' runs.

Usually we set $S^* = 0.75$ and choose $l = 1$. We also restrict α_i to be in the range $\alpha_{\rm min} = 0.01$ and $\alpha_{\rm max} = 0.75$. Choosing $\alpha_{\rm min} > 0$ has the advantage that possible noise, which might be present in the velocity representation by the particles on scales below the smoothing length still, will become damped with time. Increasing S^* can give a faster response of the artificial viscosity to the shock switch without inducing higher viscosity than necessary elsewhere. We also note that we replace α in equation (3) (and equation 8, respectively) by the arithmetic mean α_{ij} of two interacting particles. Depending on the problem, we initialize α_i at the start of a simulation either with $\alpha_{\rm min}$ or $\alpha_{\rm max}$, depending on whether or not there are already shocks present in the initial conditions, respectively.

While the approach to reduce numerical viscosity with a time-variable α_i works well with both basic parametrizations of the artificial viscosity, most of our cosmological simulations were carried out with the 'original' parametrization because the signal velocity variant became available in GADGET-2 only recently.

3 TEST SIMULATIONS

To verify that the low-viscosity formulation of SPH with its time-dependent artificial viscosity is still able to correctly capture strong shocks, we computed a number of test problems. We here report on a standard shock tube test and a spherical collapse test, which both have direct relevance for the cosmological formation of haloes. As a more advanced test for the ability of the code to follow vorticity generation, we investigate the problem of a strong shock striking an overdense cloud in a background medium. This test can also give hints whether turbulence is less strongly suppressed in the low-viscosity treatment of SPH than in the original formulation.

3.1 Shock tube test

First, we computed a shock tube problem, which is a common test for hydrodynamic numerical schemes (Sod 1978). For definiteness, a tube is divided into two halves, having density $\rho_1 = 1$ and pressure $p_1 = 1$ on the left side, and $\rho_2 = 0.125$ and $p_2 = 0.1$ on the right side, respectively. As in Sod (1978), we assume an ideal gas with $\gamma = 1.4$. To avoid oscillations in the post-shock region (note that a shock is present in the initial conditions) we initialize the viscosity values of the particles with $\alpha_{\rm max} = 0.75$. We compute the test in three dimensions and make use of periodic boundary conditions. The initial particle grid is $5 \times 5 \times 50$ on one half, and $10 \times 10 \times 100$ on the other half, implying an equal particle mass for both sides.

In Fig. 1, we show the state of the system at simulation time $t = 5$ in terms of density, velocity and internal energy with a binning which corresponds to the smoothing length for particles in the low-density region. We also include the analytical expectation for comparison. In addition, we plot the values of the artificial viscosity parameter of the particles. Clearly visible is that the viscosity is close to $\alpha_{\rm min}$ everywhere, except in the region close to the shock. We can also see how the viscosity builds up to its maximum value in the pre-shock region and decays in the post-shock region. We note that the final post-shock state of the gas agrees well with the theoretical expectation, and is indistinguishable from the case where the original viscosity parametrization is used.

3.2 Self-similar spherical collapse

A test arguably more relevant for cosmological structure formation is the self-similar, spherical collapse of a point perturbation in a homogeneous expanding background (Bertschinger 1985). This test

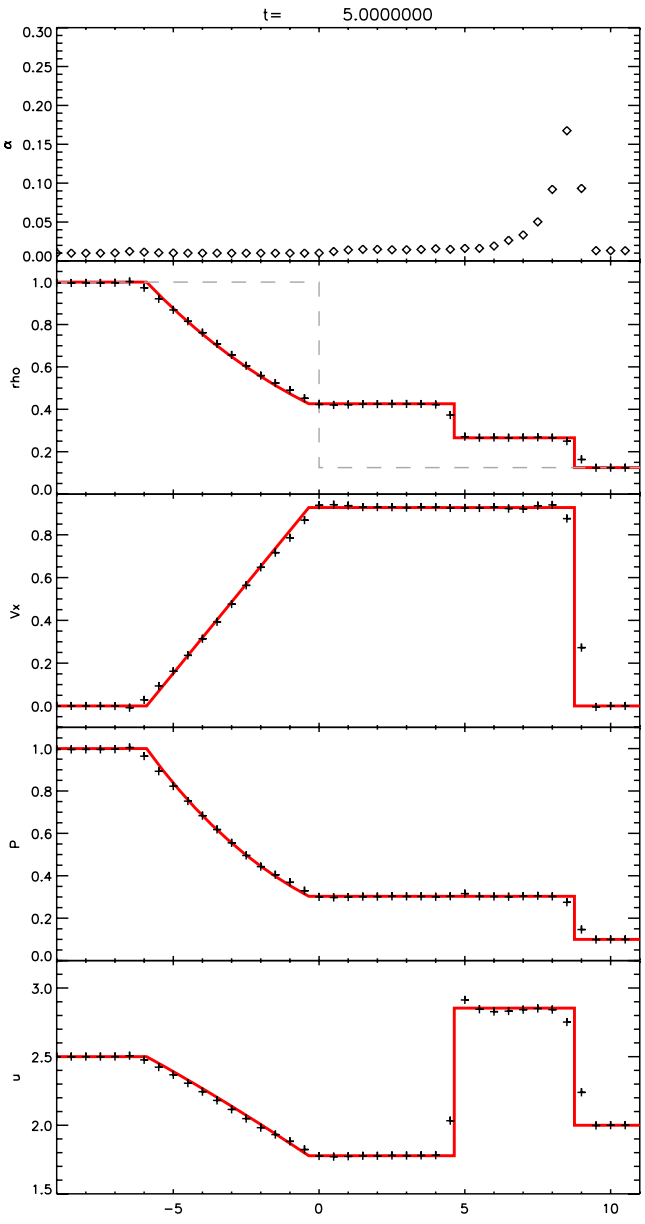

Figure 1. A standard shock tube problem (Sod 1978) computed with the low-viscosity scheme with an individual, time-dependent viscosity. From top to bottom, we show the current value of the strength of the artificial viscosity α_i, density, velocity, pressure and internal energy, averaged for bins with spacing equal to the SPH smoothing length for particles in the low-density region. The analytical solution of the problem for the time $t = 5.0$ is shown as a solid line.

is difficult for grid and SPH codes alike. The gas cloud collapses self-similarly, forming a very strong shock (which formally has infinite Mach number) at the accretion surface. While grid codes with shock capturing schemes can usually recover the sharp shock surface very well, the large dynamic range in the post-shock region with its singular density cusp, as well as the strict spherical symmetry of the problem, are challenging for mesh codes. On the other hand, Lagrangian SPH codes tend to have fewer problems with the central structure of the post-shock cloud, but they broaden the shock surface substantially, and typically show appreciable pre-shock entropy injection as result of the artificial viscosity.

We have computed the self-similar collapse test and compared the results for the new viscosity parametrization with the analytical expectation. The very strong spherical shock of this problem is a particularly interesting test, because we can here test whether the low-viscosity formulation is still able to capture the strongest shocks possible.

In Fig. 2, we show the structure of the shock at two consecutive times, scaled to the self-similar variables. In general, the SPH result recovers the analytical solution for the post-shock state very well, especially when the entropy profile is considered. However, the shock is substantially broadened, and some pre-heating in front of the shock is clearly visible. In the velocity field, some weak post-shock oscillations are noticeable. We have also indicated the smoothing lengths of the SPH particles as horizontal error bars for each of the data points (the points at which the SPH kernel falls to zero is reached at twice this length). For comparison, we additionally overplotted the analytical solution adaptively smoothed with the SPH kernel size at each bin.

The panels of the right column in Fig. 2 show the profile of the viscosity parameter, which was set to $\alpha_{\rm min}$ at the beginning of the simulation, as the initial conditions do not contain a shock. The viscosity parameter builds up immediately after starting the simulation as the strong shock forms. Later, we can see how the viscosity parameter begins to decay towards $\alpha_{\rm min}$ in the inner part, how it builds up to $\alpha_{\rm max}$ towards the shock surface, and how a characteristic profile develops as the shock moves outward. In the post-shock region, an intermediate viscosity value is maintained for some time due to some non-radial motions of gas particles in this region.

3.3 Shock–cloud interaction

To verify that the low-viscosity scheme also works in more complex hydrodynamic situations, we simulate a test problem where a strong shock strikes a gas cloud embedded at pressure equilibrium in a lower-density environment. A recent discussion of this set-up can be found in Poludnenko, Frank & Blackman (2002, and references therein). SPH is able to reproduce the main features expected in this test problem reasonably well, such as reverse and reflected shocks, back-flow, primary and secondary Mach stems, primary and secondary vortices, etc. (see Springel 2005). Our purpose here is to check whether the new scheme for a time-variable viscosity performs at least equally well as the original approach.

In Fig. 3, we compare the time evolution of the projected gas density for the original viscosity scheme (left-hand side) with the new low-viscosity scheme (right-hand side). Overall, we find that the new scheme produces quite similar results as the original method. However, there are also a number of details where the low-viscosity scheme appears to work better. One is the external reverse bow shock, which is resolved more sharply with the new scheme compared to the original one. This is consistent with our findings from the previous tests, where we could also notice that shocks tend to be resolved somewhat more sharply using the new scheme. We also note that instabilities along shear flows (e.g. the forming vortexes or the back-flow) are appearing at an earlier time, as expected if the viscosity of the numerical scheme is lower. This should help to resolve turbulence better.

In summary, the low-viscosity scheme appears to work without problems even in complex situations involving multiple shocks and vorticity generation, while it is still able to keep the advantage of a reduced viscosity in regions away from shocks. We can therefore expect this scheme to also work well in a proper environment

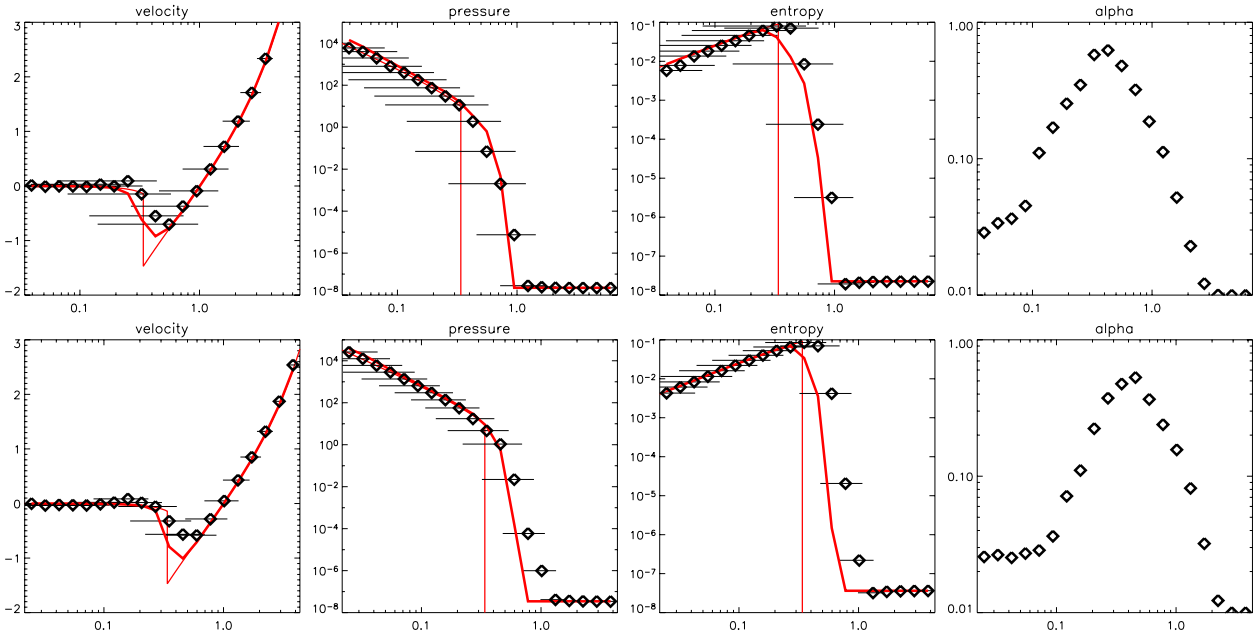

Figure 2. Profiles of velocity (left column), pressure (middle-left column) entropy (middle-right column) and viscosity constant α (right column) for the spherical collapse test at two different times (from top to bottom). The thin line marks the analytical solution, and diamonds give the result obtained by the new SPH formulation for the time-dependent viscosity. The thick line is the analytical solution adaptively smoothed with the SPH kernel, using the smoothing length of the particles in each bin. The lengths of the horizontal lines plotted at each data point correspond to the smoothing lengths of the SPH particles at this position.

of cosmological structure formation, and simulations should be able to benefit from the reduced viscosity characteristics of the scheme.

4 COSMOLOGICAL CLUSTER SIMULATIONS

We have performed high-resolution hydrodynamic simulations of the formation of nine galaxy clusters. The clusters span a mass range from $10^{14}\,h^{-1}\,\mathrm{M}_\odot$ to $2.3\times10^{15}\,h^{-1}\,\mathrm{M}_\odot$ and have originally been selected from a DM-only simulation (Yoshida, Sheth & Diaferio 2001) with box-size $479\,h^{-1}$ Mpc of a flat ΛCDM model with $\Omega_0 = 0.3$, $h = 0.7$, $\sigma_8 = 0.9$ and $\Omega_\mathrm{b} = 0.04$. Using the 'zoomed initial conditions' (ZIC) technique (Tormen, Bouchet & White 1997), we then resimulated the clusters with higher mass and force resolution by populating their Lagrangian regions in the initial conditions with more particles, adding additional small-scale power appropriately. The selection of the initial region was carried out with an iterative process, involving several low-resolution DM-only resimulations to optimize the simulated volume. The iterative cleaning process ensured that all of our clusters are free from contaminating boundary effects out to at least 3–5 virial radii. Gas was introduced in the high-resolution region by splitting each parent particle into a gas and a DM particle. The final mass-resolution of these simulations was $m_\mathrm{DM} = 1.13\times10^9\,h^{-1}\,\mathrm{M}_\odot$ and $m_\mathrm{gas} = 1.7\times10^8\,h^{-1}\,\mathrm{M}_\odot$ for DM and gas within the high-resolution region, respectively. The clusters were hence resolved with between 2×10^5 and 4×10^6 particles, depending on their final mass. For details of their properties, see Table 1. The gravitational softening length was $\epsilon = 5.0\,h^{-1}$ kpc (Plummer-equivalent), kept fixed in physical units at low redshift and switched to constant comoving softening of $\epsilon = 30.0\,h^{-1}$ kpc at $z \geqslant 5$. Additionally, we resimulated one of the smaller clusters (g676) with six times more particles, decreasing the softening by a factor of 2 to $\epsilon = 2.5\,h^{-1}$ kpc.

We computed three sets of simulations using non-radiative gas dynamics, where each cluster was simulated three times with different prescriptions for the artificial viscosity. In our first set, we used the original formulation of artificial viscosity within SPH. In the second set, we used the parametrization based on signal velocity, but with a fixed coefficient for the viscosity. Finally, in our third set, we employed the time-dependent viscosity scheme, which we expect to lead to lower residual numerical viscosity. Our simulations were all carried out with an extended version of GADGET-2 (Springel 2005), a new version of the parallel TreeSPH simulation code GADGET (Springel, Yoshida & White 2001). We note that the formulation of SPH used in this code follows the 'entropy-conserving' method proposed by Springel & Hernquist (2002).

5 IDENTIFYING TURBULENCE

In the idealized case of homogeneous and isotropic turbulence, the autocorrelation function of the velocity field of the fluid should not depend on the position (homogeneity) and it should only depend on the magnitude of the distance $\boldsymbol{r}$ between points (isotropy). The tensor of the correlation function of the velocities is thus given by (e.g. Choudhuri 1998)

$$R_{ij}(r) = \langle v_i(\boldsymbol{x}) v_j(\boldsymbol{x}+\boldsymbol{r})\rangle \tag{12}$$

where $\boldsymbol{x}$ is the position of a fluid particle. The 3D power spectral density of the turbulent field is given by (e.g. Choudhuri 1998)

$$\Phi_{ij}(\boldsymbol{k}) = \frac{1}{(2\pi)^3}\int R_{ij}(\boldsymbol{r})\exp(\mathrm{i}\,\boldsymbol{k}\boldsymbol{r})\,\mathrm{d}\,\boldsymbol{r}. \tag{13}$$

The energy spectrum, $E(k)$, associated with the fluctuations of the velocity field is related to the diagonal parts of both the tensor of the correlation function and that of the power spectral density. This

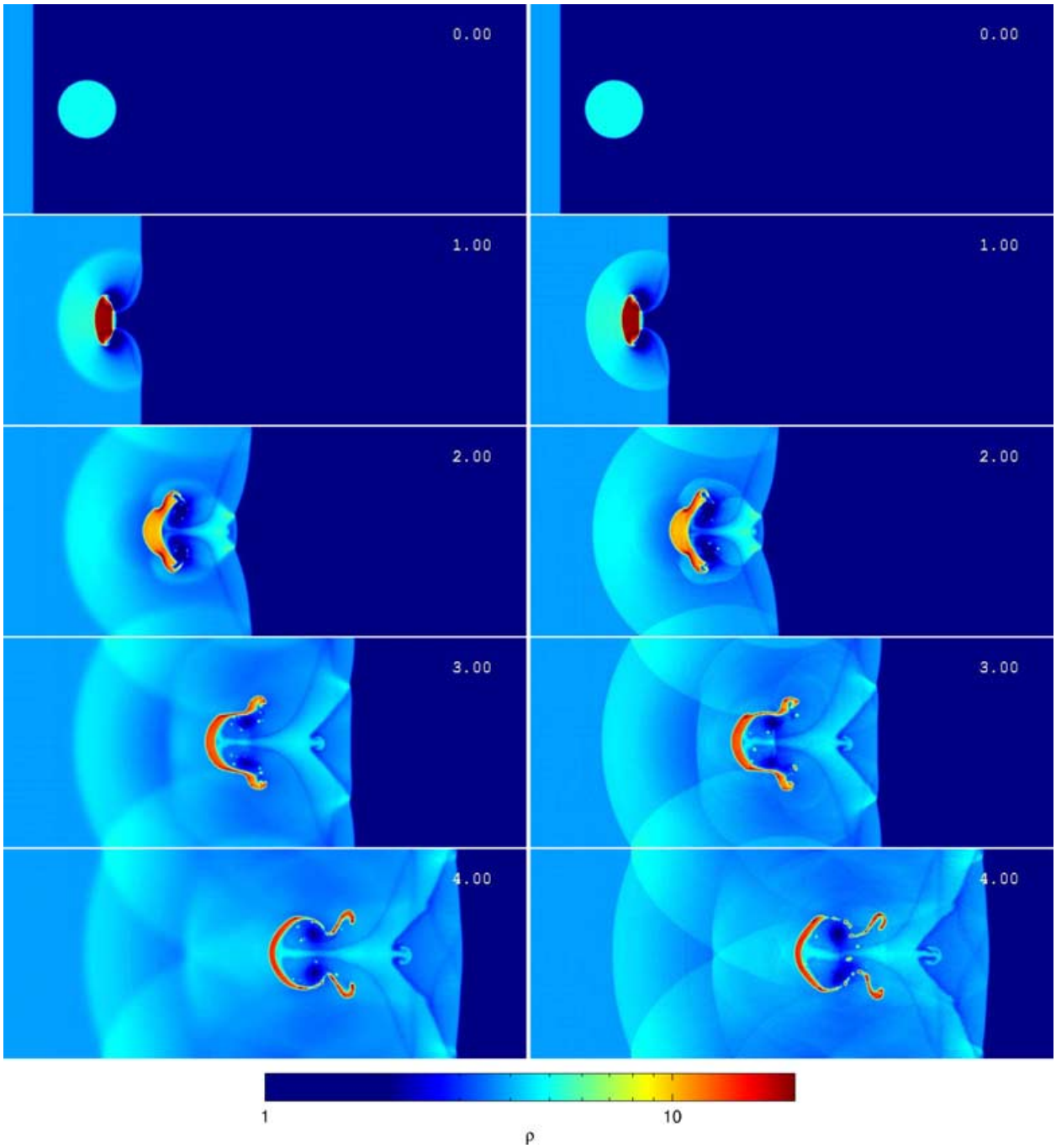

Figure 3. Time evolution of the interaction of a strong shock wave with an overdense cloud. We show the projected gas density and compare simulations carried out with original SPH (left) and the low-viscosity formulation (right). The incident shock wave has Mach number 10, and the cloud is initially at pressure equilibrium in the ambient medium and has overdensity 5.

energy spectrum is given by (e.g. Choudhuri 1998)

$$E(k) = 2\pi k^2 \Phi_{ii}(k), \tag{14}$$

and the total turbulent energy per unit mass is

$$u_{\rm turb} = \frac{1}{2}\langle v^2 \rangle = \frac{1}{2} R_{ii}(\boldsymbol{r} = 0) = \int_0^\infty E(k)\,{\rm d}k, \tag{15}$$

where the summation convention over equal indices is adopted.

The real case of the ICM is however much more complex, in particular not homogeneous and isotropic. The gravitational field induces density and temperature gradients in the ICM, and the continuous infall of substructures drives bulk motions through the ICM. These effects break both homogeneity and isotropy at some level, at least on the scale of the cluster, and thus demand a more complicated formalism to appropriately characterize the turbulent field. It is not the aim of the present paper to solve this problem completely. Instead we focus on a zero-order description of the energy stored in turbulence in the simulated boxes, and for this purpose the basic formalism described below should be sufficient.

Table 1. Main characteristics of the non-radiative galaxy cluster simulations. Column 1 gives the identification label. Columns 2 and 3 give the mass of the dark matter ($M_{\rm DM}$), columns 4 and 5 the mass of the gas ($M_{\rm gas}$) components inside the virial radius. Columns 6 and 7 give the virial radius $R_{\rm v}$. Columns 8 and 9 give the X-ray luminosity inside the virial radius $L_{\rm x}$, calculated within the (0.1–10) kev band. Columns 10 and 11 give the mass-weighted temperature ($T_{\rm MW}$), and columns 12 and 13 give the spectroscopic-like temperature ($T_{\rm sl}$).

Simulations	$M_{\rm DM}$ (h^{-1} 10^{14} M$_\odot$)		$M_{\rm GAS}$ (h^{-1} 10^{13} M$_\odot$)		$R_{\rm v}$ (h^{-1} kpc)		$L_{\rm x}$ (10^{44} erg s^{-1})		$T_{\rm MW}$(keV)		$T_{\rm sl}$(keV)	
	svisc	lvisc	svisc	lvisc	svisc	lvisc	svisc	lvisc	svisc	lvisc	svisc	lvisc
g1	14.5	14.5	17.5	17.0	2360	2355	47.1	21.3	7.2	7.1	5.8	5.6
g8	22.6	22.4	19.8	19.8	2712	2705	63.1	32.1	9.3	9.1	6.2	5.7
g51	13.0	13.0	11.5	11.5	2255	2251	30.8	17.9	6.4	6.3	4.6	4.7
g72	13.5	13.4	12.0	11.9	2286	2280	18.3	14.1	5.8	5.8	4.0	4.0
g676	1.1	1.0	0.95	0.91	983	972	3.2	1.4	1.3	1.3	1.6	1.5
g914	1.2	1.0	1.07	0.91	1023	971	4.2	1.7	1.4	1.3	1.6	1.7
g1542	1.1	1.0	0.95	0.90	982	967	3.0	1.4	1.3	1.2	1.4	1.5
g3344	1.1	1.1	1.00	0.96	1002	993	2.2	1.4	1.4	1.3	1.4	1.5
g6212	1.1	1.1	1.00	1.01	1000	1006	3.0	1.5	1.3	1.3	1.6	1.7

A crucial issue in describing turbulent fields in the ICM is the distinction between large-scale coherent velocity field and small-scale 'random' motions. Unfortunately, the definition of a suitable mean velocity field is not unambiguous because the involved scale of averaging introduces a certain degree of arbitrariness. Perhaps the simplest possible procedure is to take the mean velocity computed for the cluster volume (calculated, for example, within a sphere of radius $R_{\rm vir}$) as the coherent velocity field, and then to define the turbulent velocity component as a residual to this velocity. This simple approach (hereafter, standard approach) has been widely employed in previous works (e.g. Norman & Bryan 1999; Sunyaev, Norman & Bryan 2003), and has led to the identification of ICM turbulence in these studies. However, an obvious problem with this method is that this global subtraction fails to distinguish a pure laminar bulk flow from a turbulent pattern of motion. Note that such large-scale laminar flows are quite common in cosmological simulations, where the growth of clusters causes frequent infalls and accretions of subhaloes. This infall of substructures is presumably one of the primary injection mechanisms of ICM turbulence.

To avoid this problem, a mean velocity field smoothed on scales smaller than the whole box can be used, and then the field of velocity fluctuation is defined by subtracting this mean-local velocity, $\overline{\boldsymbol{v}}(\boldsymbol{x})$, from the individual velocities $\boldsymbol{v}_i$ of each gas particle. We note that if the smoothing scale is chosen too small, one may risk losing large eddies in the system if they are present, but at least this procedure does not overestimate the level of turbulence.

Following this second approach (hereafter, local velocity approach), we construct a mean local velocity field $\overline{\boldsymbol{v}}(x)$ on a uniform mesh by assigning the individual particles to a mesh with a triangular shape cloud (TSC) window function. The mesh covers a region of 1.0 comoving Mpc on a side and typically has between 8^3 and 64^3 cells, which is coarse enough to avoid undersampling effects. The equivalent width of the TSC kernel is approximately three grid cells in each dimension, corresponding to a smoothing scale of $\approx$ 360–45 kpc, respectively. As our analysis is restricted only to the highest-density region in the clusters, the scale for the TSC smoothing is always larger than the SPH smoothing lengths for the gas particles, which typically span the range 7.5–15 h^{-1} kpc in the box we consider.

We then evaluate the local velocity dispersion at the position $\boldsymbol{x}$ of each mesh cell over all particles a in the cell by

$$\sigma^2_{ij}(\boldsymbol{x}) \simeq \langle [v_{a,i} - \bar{v}_i(\boldsymbol{x})][v_{a,j} - \bar{v}_j(\boldsymbol{x})] \rangle_{\rm cell}, \qquad (16)$$

where i and j are the indices for the three spatial coordinates, and $\langle\rangle_{\rm cell}$ denotes the average over particles within each cell. The diagonal part of the tensor of the correlation function of the field of velocity fluctuations at $r = 0$ in the simulated box can then be approximated by

$$R_{ii}(r=0) \simeq \left\langle \sigma^2_{ii}(\boldsymbol{x}) \right\rangle_{\rm Box}. \qquad (17)$$

Based on equation (15), we can then estimate the energy density of the turbulence in real space as

$$\rho(\boldsymbol{x}) \int E(k)\,{\rm d}k \sim \frac{1}{2}\rho(\boldsymbol{x}) \times \begin{cases} \left\langle \sigma^2_{ii}(\boldsymbol{x}) \right\rangle_{\rm box}, \\ \left\langle v^2_i(\boldsymbol{x}) \right\rangle_{\rm box}, \end{cases} \qquad (18)$$

in the local velocity and standard cases, respectively. Here $\rho(\boldsymbol{x})$ is the gas density within the cells.

The subtraction of a local velocity from the velocity distribution of the particles is expected to efficiently filter out the contribution from laminar bulk flows with a scale $\geqslant$ three times the size of the cells used in the TSC smoothing. However, a large-scale turbulent velocity field component, if it exists, would also be suppressed, so that this procedure can be expected to reduce the turbulent velocity field to a certain degree. As shown in Fig. 4, this depends on the resolution of the mesh used in the TSC assignment. Fig. 4 shows that the increase of the turbulent velocity dispersion with the cell size is not dramatic for cell sizes larger than 100 kpc. We find that (Vazza et al., in preparation) a TSC smoothing with larger cell sizes would not efficiently filter out contributions from laminar bulk motions. It can be tentatively concluded that the local velocity approach with a smoothing with 16^3–32^3 cells in the central (1.0 Mpc)^3 volume catches the bulk of the turbulent velocity field in the simulated box. Therefore, if not specified otherwise, all the numerical quantities given in the following are obtained using a TSC-assignment procedure based on 32^3 cells. A more detailed discussion of this method and tests of the parameters involved is reported elsewhere (Vazza et al., in preparation).

Figs 5 and 6 give examples of the turbulent velocity field calculated with both the standard and local velocity methods, showing the same galaxy cluster in both cases, but in one case simulated with the signal-velocity variant of the viscosity, and in the other with the new time-dependent low-viscosity scheme. Note that we here selected a situation where a large (ca. 500 kpc long) laminar flow pattern can be easily identified close to the centre of one of our simulated clusters (g72). When the mean cluster velocity field is subtracted as in Fig. 5, large residual bulk flow patterns remain visible, caused by a substructure moving through the cluster atmosphere. We colour-coded the turbulent kinetic energy of particles, $E_{\rm t}(\boldsymbol{x}) \sim 1/2\,\rho(\boldsymbol{x})\sigma_v(\boldsymbol{x})^2$, after subtracting the local mean velocity

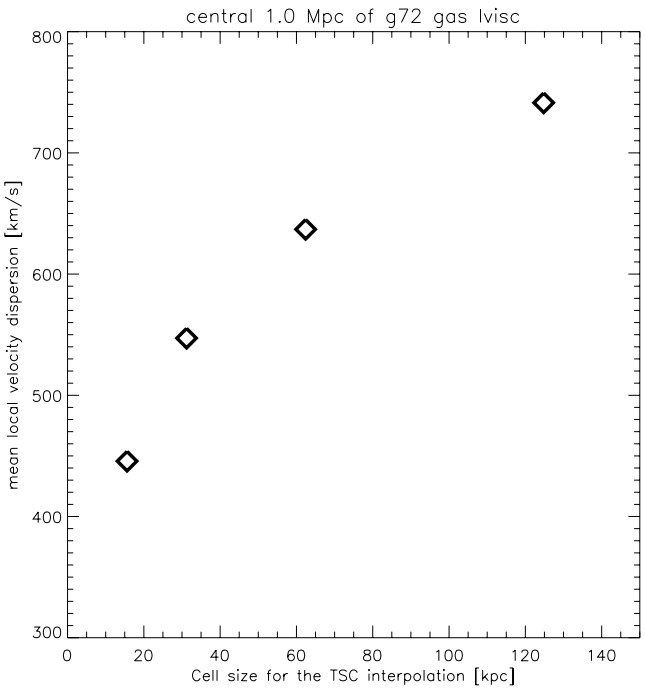

Figure 4. Mean local velocity dispersion for the central 500^3 kpc^3 box as a function of the resolution adopted for the TSC smoothing of the local mean field. Results are plotted for a low-viscosity simulation.

field (here smoothed on to a 64^3 mesh) for the upper panels and after subtracting the global mean bulk velocity of the cluster for the lower panels. We can see that fluid instabilities of KH type are growing along the interfaces of the large laminar flow pattern, visible in the upper-left panel. As expected, the strength of this turbulent velocity field is considerably larger in the simulation obtained with the new low-viscosity scheme, providing evidence that such instabilities are less strongly damped in this scheme. This can also be seen by the longer flow field lines in Fig. 6. Fig. 5 also visually confirms the differences in the two approaches of filtering the velocity field. Whereas the local velocity approach highlights the energy within the velocity structure along boundary layers, the energy within the large, bulk motions is preferentially selected when only subtracting the global mean bulk velocity.

The total cumulative kinetic energy in the random gas motions inside our mesh (centred on the cluster centre) reaches 5–30 per cent of the thermal energy for the simulations using the new, low-viscosity scheme, whereas it remains at much lower levels (≈2–10 per cent) when the signal velocity parametrization of the viscosity is used. If the original viscosity scheme is used, it is typically at even lower values (≈1–5 per cent).

In general, we find that more massive clusters tend to have a higher fraction of turbulent energy content. However, given that our simulations have fixed mass resolution, this trend could in principle simply reflect a numerical resolution effect. In order to obtain further information on this, we have resimulated one of the smaller clusters (g676) with six times better mass resolution using the signal velocity parametrization of the viscosity. At $z = 0$, this cluster is then resolved by nearly as many particles as the massive clusters simulated with our standard resolution. We find that for this high-resolution simulation the level of turbulence (≈3 per cent) is increased compared with the normal resolution (≈2 per cent), but it remains less compared to what we found for the low-viscosity scheme at our normal resolution (≈5 per cent). This confirms two expectations. First, the low-viscosity scheme effectively increases the resolution on which SPH simulations can resolve small-scale velocity structure, which otherwise becomes already suppressed on scales larger than the smoothing length by spurious viscous damping effects due to the artificial viscosity. Secondly, the amount of turbulence in the high-resolution version of g676 is still less than what we find with the same viscosity implementation in the larger systems, and even much smaller than what we find with the low-viscosity scheme in the large clusters. This tentatively suggests that the trend of a mass dependence of the importance of turbulence is not caused by numerical effects. Note that with a fixed physical scale of 1 Mpc we are sampling different fractions of $R_{\rm vir}$ in clusters of different masses. However, if, in case of the less massive system, we restrict the sampling relative to $R_{\rm vir}$ to measure within comparable volumes, the fraction of turbulent energy content found in the small cluster increases roughly by a factor of 2. Thereby, we still find a significant trend with mass when measuring turbulence within a fixed fraction of $R_{\rm vir}$. Although it should be mentioned that unless the dissipation of turbulence on small scales will be modelled correctly in a physical granted way, the different formation time-scales of systems with different masses can potentially also contribute to such a trend.

In order to verify that our method for measuring the local velocity dispersion gives reasonable values, Fig. 7 shows a radial profile of the volume-weighted, relative difference between thermal pressure for the signal velocity based and low-viscosity run. Here we used an average over the three massive clusters (g1, g51 and g72) which have comparable masses. The solid line shows the relative difference in radial shells and indicates that the turbulent pressure support can reach even up to 50 per cent in the central part and drops to 0 at approximately $0.2R_{\rm vir}$. The dashed line shows the cumulative difference, which over the total cluster volume contributes between 2 and 5 per cent to the total pressure. The diamonds mark the measurement inferred from the local velocity dispersion within centred boxes of various sizes. We also calculate the difference between the signal velocity based and low-viscosity runs using the mean values over the three clusters. Qualitatively, there is good agreement of results obtained with this approach with the cumulative curve. This confirms that our method to infer the turbulent energy content from the local velocity dispersion of the gas is meaningful. Note that the temperature which is used to calculate the pressure is determined by strong shock heating. As different resimulations of the same object can lead to small (but in this context non-negligible) timing differences, this can introduce sizable variations in the calculated pressure, especially during merging events. We verified that these differences for individual clusters are significantly larger than the differences between the cumulative curve (dashed line) and the data points from the local velocity dispersion (diamonds). Therefore, we can only say that the two methods agree well within their uncertainties.

Finally, the inset of Fig. 7 gives the absolute contribution from the low viscosity and the original viscosity in its two variants using the local velocity dispersion. It seems that using the signal based viscosity in general leads already to more turbulence than the 'old' original viscosity, but the time-dependent treatment of the viscosity works even more efficiently.

Although we are using a formalism which is suitable only for isotropic and homogeneous turbulence, the study of the turbulent energy spectrum may provide some useful insight. In the local mean velocity approach, we can obtain the diagonal part of the turbulent

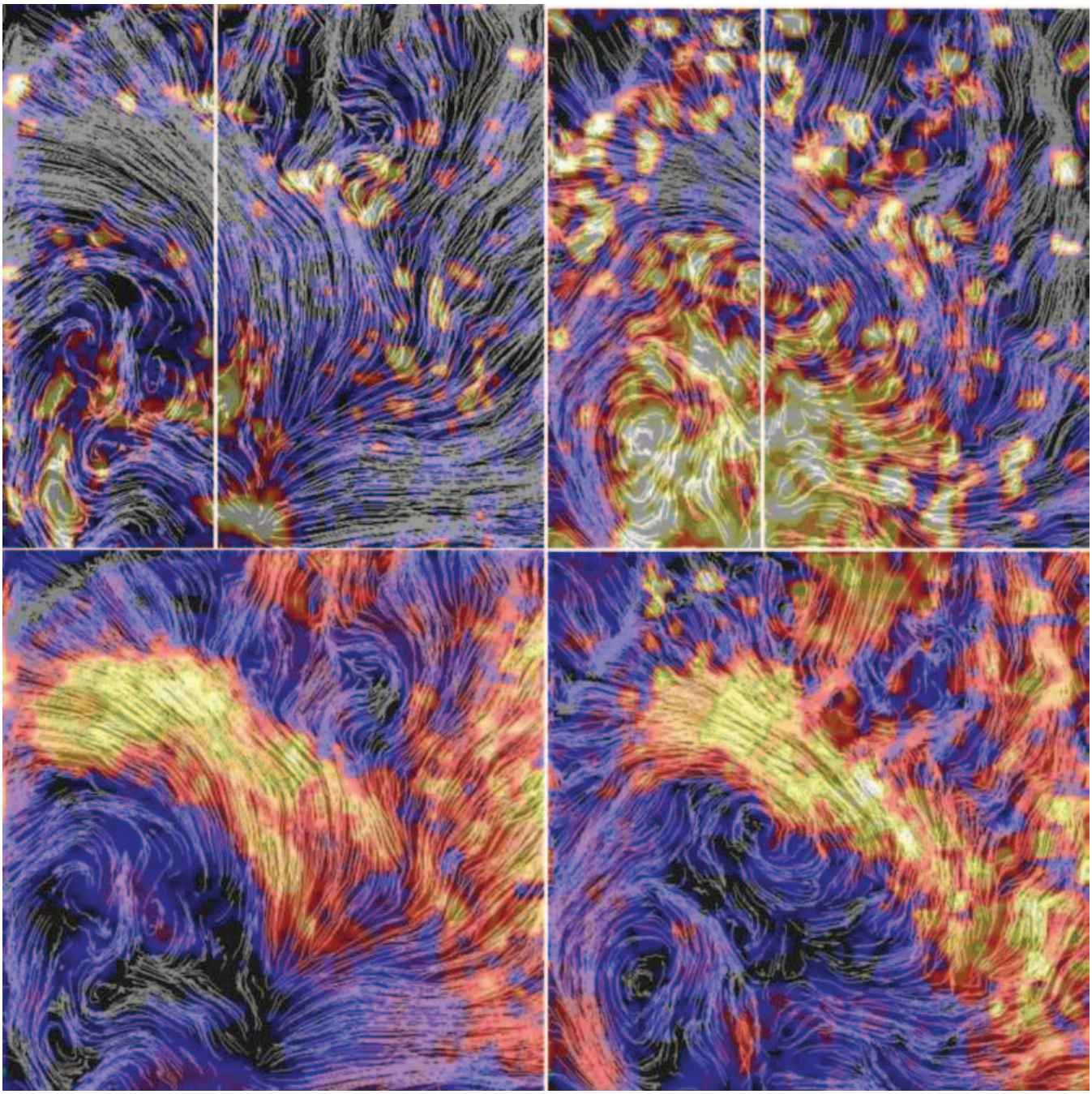

Figure 5. Gas velocity field in a slice through the central Mpc of a cluster simulation g72 after subtracting the global mean bulk velocity of the cluster. The panels on the left are for a run with the original viscosity of SPH while the panels on the right show the result for the low-viscosity scheme. The underlying colour maps represent the ratio of turbulent kinetic energy and total kinetic energy content of particles, inferred using the local velocity method (upper row) or the standard velocity method (lower row). Thereby yellow corresponds to a ratio close to one. For the local velocity method a conservative 64^3 grid is used in the TSC smoothing. The cluster centre is just below the lower-left corner of the images. The vertical lines in the upper row show where the one-dimensional profiles for the simulated radio emission of Fig. 19 are taken.

energy spectrum using equation (13), with R_{ii} approximated as

$$R_{ii}(r) = \langle [v_{a,i} - \overline{v}_i(\boldsymbol{x}_a)][v_{b,i} - \overline{v}_i(\boldsymbol{x}_b)] \rangle_{\rm box}, \qquad (19)$$

where $\overline{\boldsymbol{v}}(\boldsymbol{x}_a)$ is the TSC-mean velocity of the cell which contains the point $\boldsymbol{x}_a$, and the average is over all pairs (a, b) in the box with a certain distance r. In the standard approach, we would here subtract the centre-of-mass velocity of the cluster instead.

A major problem for estimating the correlation functions $R_{ii}(r)$ in this way, and with the energy spectrum calculated from SPH simulations (and in general from adaptive resolution approaches), is given by the non-uniform sampling of the point masses in the simulated box. To reduce this problem we focus on regions corresponding to the cores of galaxy clusters. Here the requirement of isotropic and homogeneous turbulence is hopefully better fulfilled.

© 2005 The Authors. Journal compilation © 2005 RAS, MNRAS **364,** 753–772

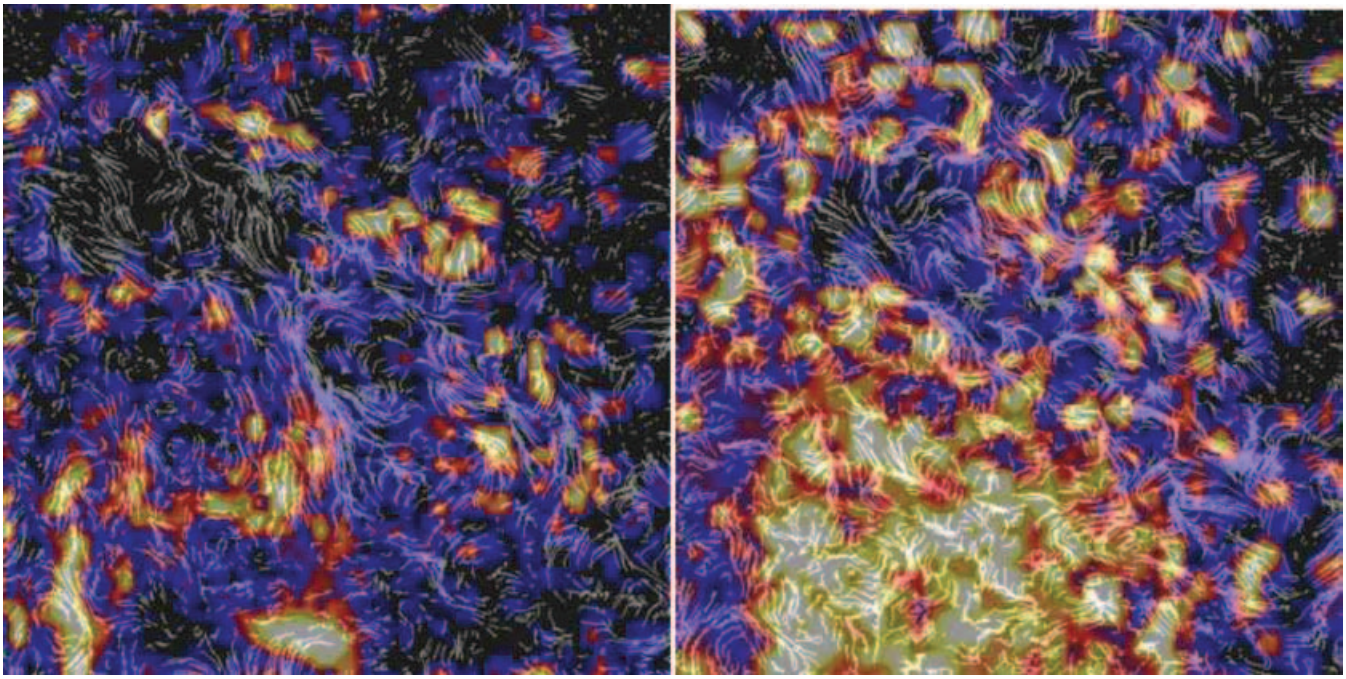

Figure 6. The same slice of the gas velocity field as in Fig. 5 of cluster g72 after subtracting the local mean velocity of the cluster. The panel on the left is for a run with the original viscosity of SPH while the panel on the right shows the result for the low-viscosity scheme.

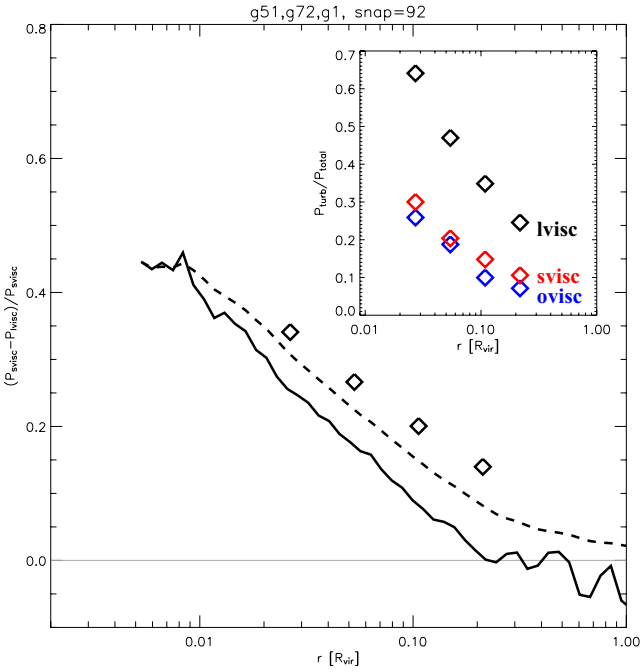

Figure 7. Radial profile of the relative thermal pressure difference averaged over three nearly equally massive clusters (g1, g51 and g72), comparing the signal velocity based and low-viscosity runs (lines). The dashed line is the cumulative difference, whereas the solid line marks the profile in radial shells. The diamonds mark the difference in the turbulent energy support we inferred from the local velocity dispersion within several concentric cubes of different sizes ($l_{\rm cube} = 2r$) for the same runs. This should be compared with the dashed line. The inset shows the absolute value inferred from the local velocity dispersion from the different viscosity parametrizations, respectively.

Also the density profile is relatively flat such that the sampling with gas particles is not too non-uniform. In addition, we estimate the correlation function as an average of dozens of Monte Carlo extractions of gas particles from the simulated output, where we picked one particle from each of the $(15.6\ {\rm kpc})^3$ cells in order to have a uniform, volume-weighted set of particles.

In Fig. 8, we show examples for the energy spectra we obtained for the two approaches by Fourier transforming the measurements for $R_{ii}\,(r)$. The energy spectra for the two methods for treating the mean velocities are reasonably similar in shape, but the spectrum calculated with the local mean velocity has a lower normalization, independent of resolution. This is expected because the TSC smoothing filters out contributions from laminar motions, and may also damp the turbulent field at some level. Both spectra show a slope nearly as steep as a Kolmogorov spectrum [which has $E(k) \propto k^{-5/3}$] at intermediate scales, but exhibit a significant flattening at smaller scales (i.e. large k). The flattening at small scales could be caused by numerical effects inherent in the SPH technique, where an efficient energy transfer to small-scale turbulent cells on scales approaching the numerical resolution is prevented, and thus a complete cascade cannot develop. Additionally, the lack of numerical viscosity in the low-viscosity scheme can in principle lead to an increase of the noise level within the velocity field representation by the SPH particles on scales below the smoothing length. Such noise in general could contribute to the flattening at small scales. It is however not clear how to separate this noise component from a turbulent cascade reaching scales similar or below the smoothing length. Therefore, one focus of future investigations has clearly to be towards this issue. It is however important to note that the largest turbulent energy content (especially at small scales) is always found in the clusters simulated with the low-viscosity scheme. This is particularly apparent in the energy spectra when the local velocity approach is used and suggests that the energy spectrum obtained with the standard approach is significantly affected by laminar bulk flows, which are not sensitive to a change in parametrization of the artificial viscosity.

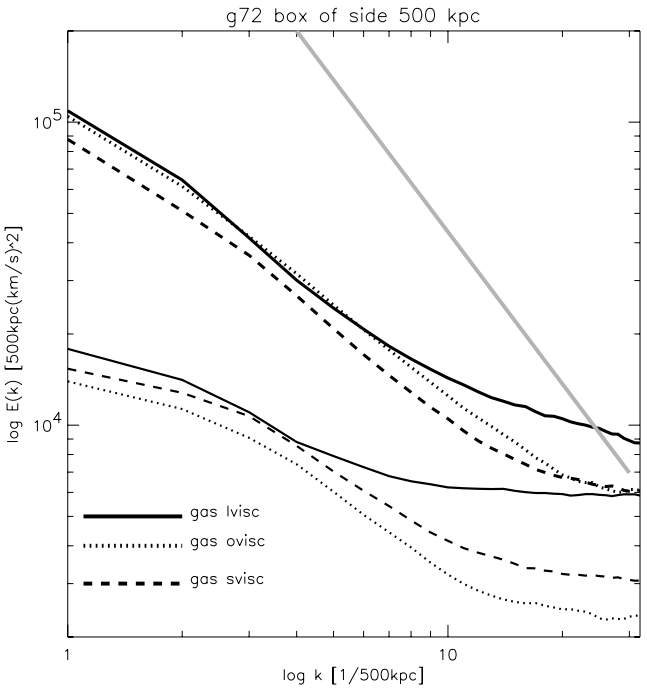

Figure 8. The energy spectra of the standard velocity fluctuations (upper curves) and of the local velocity fluctuations (lower curves) of gas particles in the central 500^3 kpc^3 region of a cluster simulated with the original recipe for the artificial viscosity, with signal velocity and with the low-viscosity implementation. Additionally a Kolmogorov slope (dot-dot-dashed line) is drawn for comparison.

6 CLUSTER PROPERTIES

Different levels of small-scale random gas motions within the ICM have only mild effects on global properties of clusters such as mass or temperature, as evidenced by the measurements in Table 1. However, additional kinetic energy in turbulent motions changes the central density and entropy structure, which in turn has a sizable effect on the X-ray luminosity. We investigate the resulting changes in cluster scaling relations and radial profiles in more detail within this section.

6.1 Maps

The presence of a significant turbulent energy component in the ICM manifests itself in a modification of the balance between the gravitational potential and the gas pressure. There are in fact observational reports that claim to have detected such fluctuations in pressure maps derived from X-ray observations (Schuecker et al. 2004). We here calculate artificial pressure $P_{\rm art}$ maps for our simulations, based on surface brightness maps ($L_{\rm x}$) and spectroscopic-like (Mazzotta et al. 2004) temperature ($T_{\rm sl}$) maps. This allows artificial pressure maps to be estimated as

$$P_{\rm art} = n\, T_{\rm sl}, \tag{20}$$

where we defined

$$n = (L_{\rm x}/\sqrt{T_{\rm sl}})^{1/2}. \tag{21}$$

Figs 9 and 10 show a comparison of a number of cluster maps produced using an unsharp-mask technique of the form

$$\mathrm{Image}_{\rm unsharpmask} = \mathrm{Image} - \mathrm{Smoothed}(\mathrm{Image}, \sigma), \tag{22}$$

where a Gaussian smoothing with FWHM of $\sigma = 200$ kpc was applied. We analyse maps of the X-ray surface brightness, spectroscopic-like temperature, 'true' pressure maps (e.g. based on Compton y) and artificial pressure maps constructed as described above. All maps show the central 2 Mpc of the cluster run g1, simulated with the low-viscosity scheme (right panels) compared with the original SPH scheme (left panels).

Disregarding the large contribution by substructure in all the X-ray related maps (therefore also in the artificial pressure map), all types of maps show clear signs of turbulence. It is noticeable in both runs, but it has a much larger extent and intensity in the the low-viscosity run. Note in particular the turbulent motions (appearing as lumpiness in the unsharp-mask images) in the wake of infalling substructures, and the earlier breakup of fluid interfaces when the new, reduced viscosity scheme is used.

Pressure maps – and therefore Sunyaev–Zel'dovich (SZ) maps – are arguably the most promising type of map when searching for observational imprints of turbulence. Apart from reflecting the large-scale shape of the cluster they are known to be relatively featureless, because most of the substructures in clusters are in pressure equilibrium with their local surroundings, making them in principle invisible in pressure maps. On the other hand, the contribution of the turbulent motion to the local pressure balance can be expected to leave visible fluctuations in the thermal pressure map. This can indeed be seen nicely in the pressure (e.g. SZ) maps in Fig. 10. Note that the amplitudes of the turbulent fluctuations in the case of the low-viscosity run are larger and also spatially more extended in the core of the cluster. Artificial pressure maps constructed from the X-ray observables still show such fluctuations, but they are partially swamped by the signatures of the infalling substructures, making it difficult to quantify the amount of turbulence present in clusters using such X-ray based artificial pressure maps.

The small displacements seen in the substructure positions between the two runs are due to small differences in their orbital phases. Besides the general problem to precisely synchronize cluster simulations with different dynamical processes involved, it is well known (e.g. Tormen, Moscardini & Yoshida 2004; Puchwein et al. 2005) that the interaction of the gas with its environment can significantly change the orbits of infalling substructure. The different efficiencies in stripping the gas from the infalling substructure in the simulations with different viscosity prescription can therefore lead to small differences in the timing and orbits between the two simulations.

6.2 Scaling relations

In Fig. 11, we compare the mass-weighted temperature of our galaxy clusters for simulations with the original viscosity and for runs with the low-viscosity scheme. There are no significant changes. Comparing the X-ray luminosity instead, we find that it drops significantly by a factor of $\approx$2 for clusters simulated with the low-viscosity scheme, as shown in Fig. 12. Thereby, the X-ray luminosity is calculated within an energy band of (0.1–10.0) keV. As the simulations do not include the effect of radiative cooling and feedback, we included all particles from the simulations in the analysis. This difference in X-ray luminosity is quite interesting in the context of the long-standing problem of trying to reproduce the observed cluster scaling relations in simulations. In particular, since non-radiative cluster simulations tend to produce an excess of X-ray luminosity, this effect would help. However, it must be kept in mind that the inclusion of additional physical processes such as radiative cooling and feedback from star formation can have an even larger impact

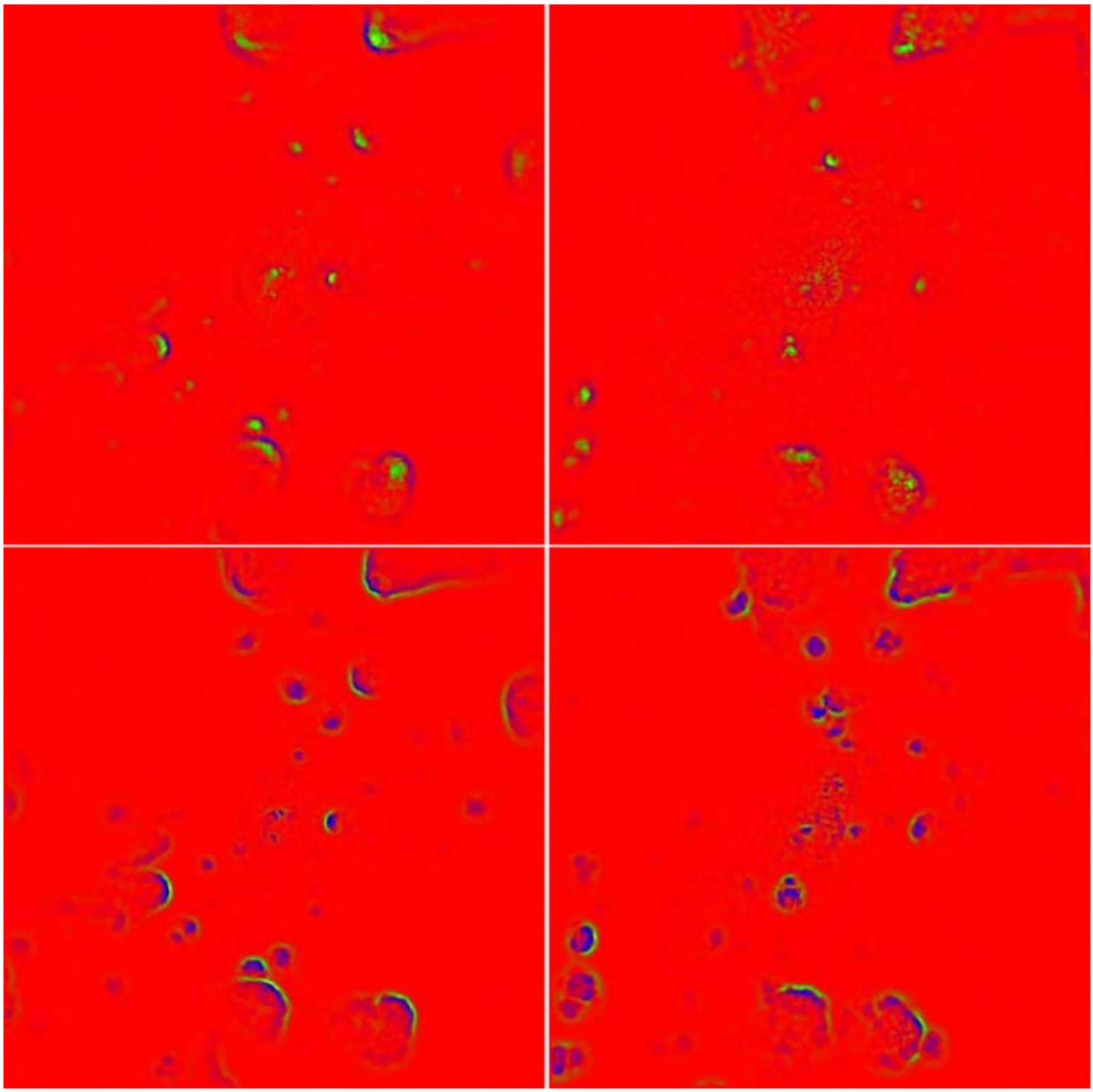

Figure 9. Unsharp mask images of X-ray maps for one of the massive clusters (g1), comparing runs with the low-viscosity scheme (right panels) with the original SPH scheme (left panels). The colours blue, red and green indicate negative, zero and positive residuals, respectively. The top row gives maps of surface brightness, while the bottom row compares maps of the 'spectroscopic-like' temperature, both within 2 Mpc centred on the cluster. We can see evidence for an increased level of turbulent motions behind the infalling substructures, and a breakup of fluid interfaces for the reduced viscosity scheme is clearly visible. Also, there is a general increase of turbulence (appearing as lumpiness) towards the centre. However, the most prominent signals in the map stem from the higher density or different temperature of substructures relative to their surrounding, or from shocks and contact discontinuities. For this reason, turbulence can be better identified in pressure maps (see Fig. 10).

on the cluster luminosity, depending on cluster mass, so a definite assessment of the scaling relation issue has to await simulations that also include these effects. Note that the difference between the two sets of simulations varies slightly from cluster to cluster. It is worth mentioning that the clusters with the smallest differences are the two systems which are the dynamically youngest within the two mass ranges. We also note that if we take a relaxed system out of the set we find that the differences in X-ray luminosity grow with time before they slowly converge to a factor of 2 in difference. This behaviour should be related to the fact that the turbulence builds up with a delay to the merging events, when the core of the substructure is subsequently destroyed by sloshing within the potential well of the cluster. Note that this delay between the start of the merger event and the build up of the chaotic motion was already noticed in the study of colliding galaxy clusters (e.g. Roettiger et al. 1997; Roettiger et al. 1999; Takizawa 2005).

6.3 Radial profiles

The presence of turbulence manifests itself in an increase of the velocity dispersion of the cluster gas, especially towards the centre,

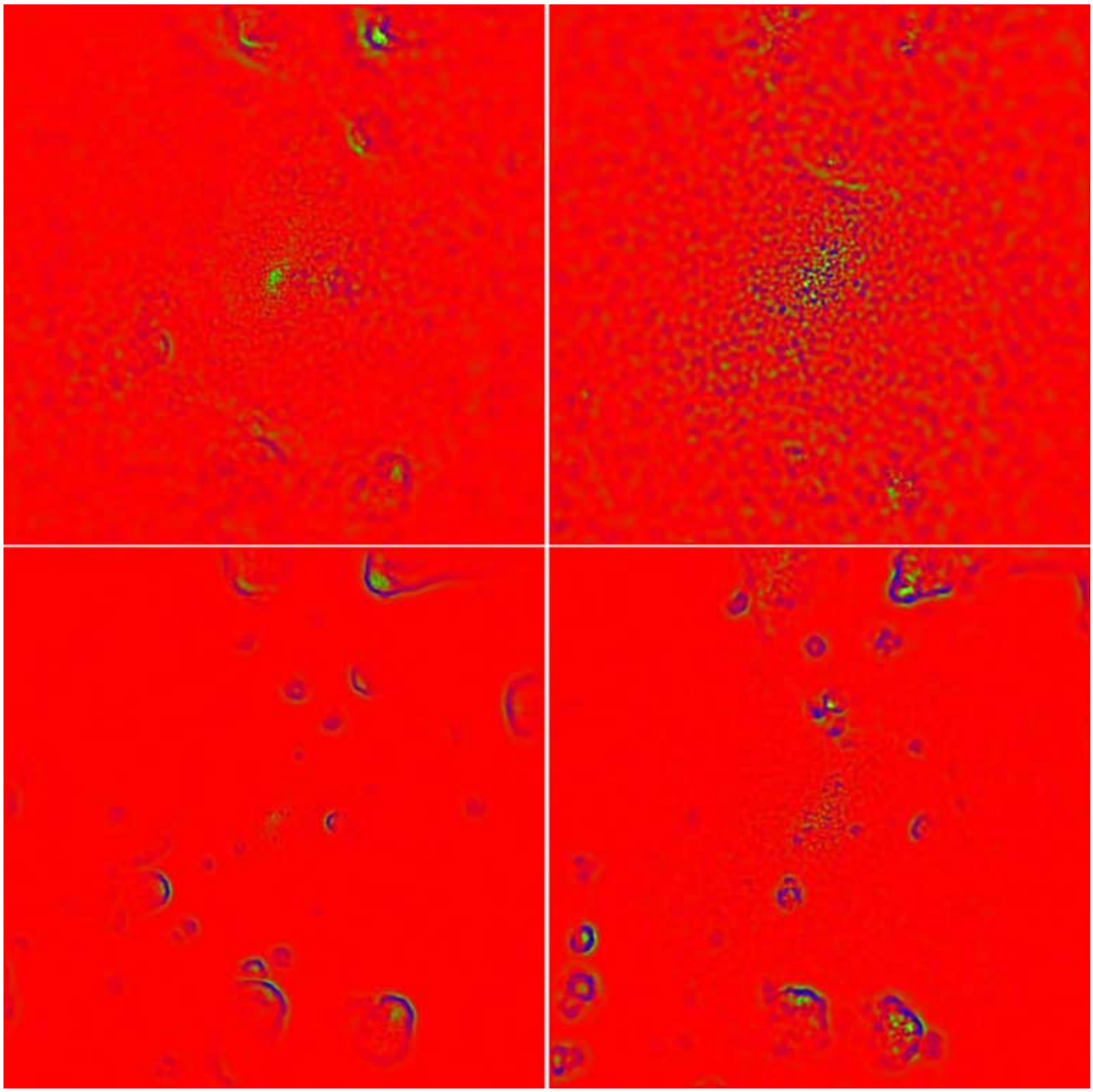

Figure 10. Unsharp mask images of pressure maps of one of the massive clusters (g1), comparing runs with the low-viscosity scheme (right panels) with the original SPH scheme (left panels). The colours blue, red and green indicate negative, zero and positive residuals, respectively. We also compare different methods for determining the pressure maps. The panels of the top row show Compton-y maps (which can be associated with projected, thermal pressure maps), whereas the maps in the bottom row are pressure maps derived based on X-ray surface brightness and spectroscopic temperature maps (see equations 20 and 21). Both kinds of maps show an increase of structure (lumpiness) for the simulation which uses the reduced viscosity scheme (right panels) when compared with the original SPH viscosity scheme (left panels). The maps based on X-ray observables show a larger degree of lumpiness due to the gas around substructures, especially in the vicinity of infalling subgroups.

while the DM velocity dispersion should be unaffected. In Fig. 13, we compare the velocity dispersion of gas and DM, averaged over the low- and high-mass clusters in our set. As expected, the velocity dispersion of the DM does not change in the low-viscosity simulations, where a larger degree of turbulence is present in the ICM. On the other hand, the central velocity dispersion of the gas increases, reaching of the order of 400 km s^{-1} for our massive clusters. As the gas is in pressure equilibrium with the unchanged gravitational potential, the hydrodynamic gas pressure will be correspondingly lower in the centre due to the presence of these random gas motions.

In Fig. 14, we show the mean cluster temperature profiles, which only shows a very mild trend of increasing temperature in the central part of clusters when using the new, low-viscosity scheme. However, the central gas density drops significantly in the low-viscosity scheme, as shown in Fig. 15. This change in density is restricted to inner parts of the cluster, roughly to within $0.1R_{\rm vir}$, which may be taken as an indication of the size of the region where turbulent motions are important.

Quite interestingly, the presence of turbulence also changes the entropy profiles. In Fig. 16, we show the radial entropy profiles of

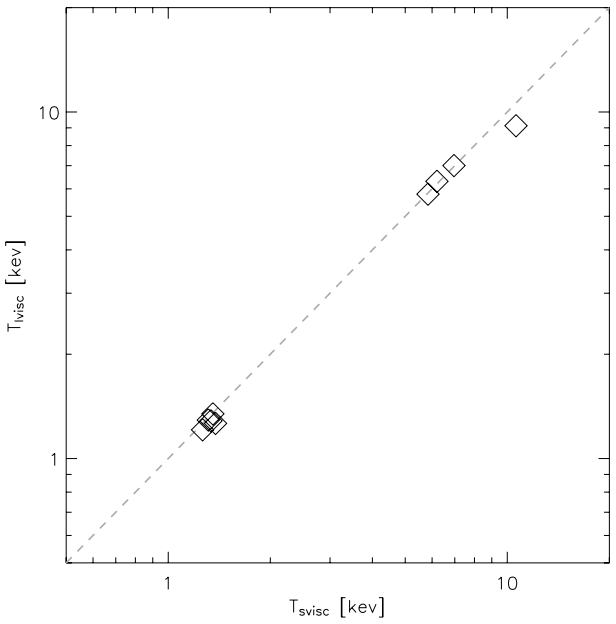

Figure 11. Comparison of the virial temperature of the nine clusters when different parametrizations of the viscosity are employed. The solid line marks the one-to-one correspondence.

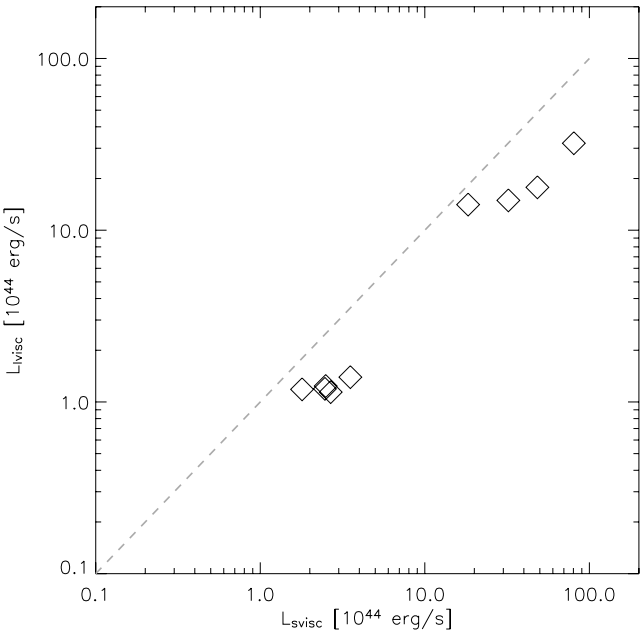

Figure 12. Comparison of the bolometric luminosity of the nine clusters when different parametrizations of the viscosity are employed. The solid line marks the one-to-one correspondence. It is evident that clusters with a larger degree of turbulence have a lower luminosity.

our clusters, which in the case of the low-viscosity scheme exhibit an elevated level of entropy in the core, with a flattening similar to that inferred from X-ray observations. It is remarkable that this central increase of entropy occurs despite the fact that the source of entropy generation, the artificial viscosity, is in principle less efficient in the low-viscosity scheme. There are two main possibilities that could explain this result. Either the low-viscosity scheme allows shocks to penetrate deeper into the core of the cluster and its progenitors such

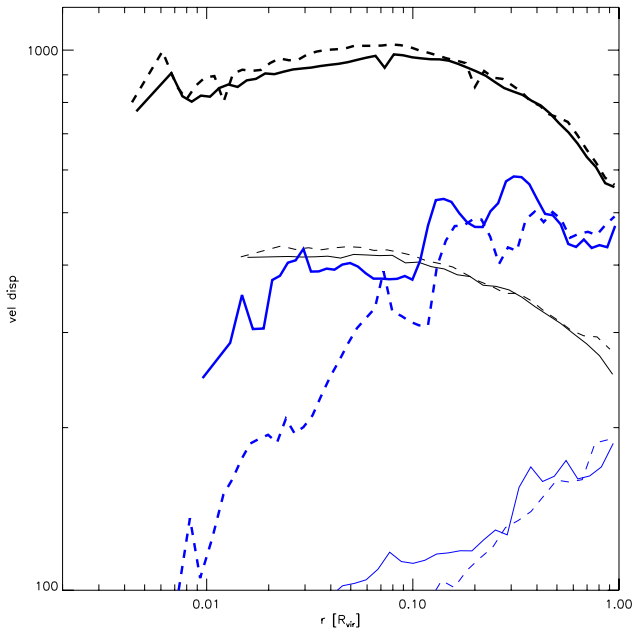

Figure 13. Radial velocity dispersion profile for DM (black) and gas (blue) particles. The thick lines represent the average over the four massive clusters, whereas the thin lines give the average over the five low-mass systems. The dashed lines are drawn from the original viscosity simulations, and the solid lines from the low-viscosity simulations.

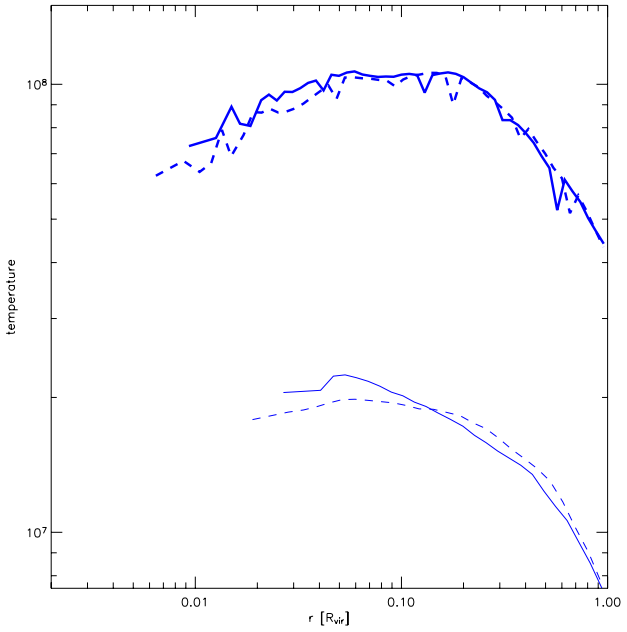

Figure 14. Mass-weighted gas temperature profile. The thick lines represent the average over the four massive clusters, whereas the thin lines give the average over the five low-mass systems. The dashed lines are drawn from the original viscosity simulations, and the solid lines from the low-viscosity simulations.

that more efficient entropy production in shocks occurs there, or, alternatively, the reduced numerical viscosity changes the mixing processes of infalling material, allowing higher entropy material that falls in late to end up near the cluster centre.

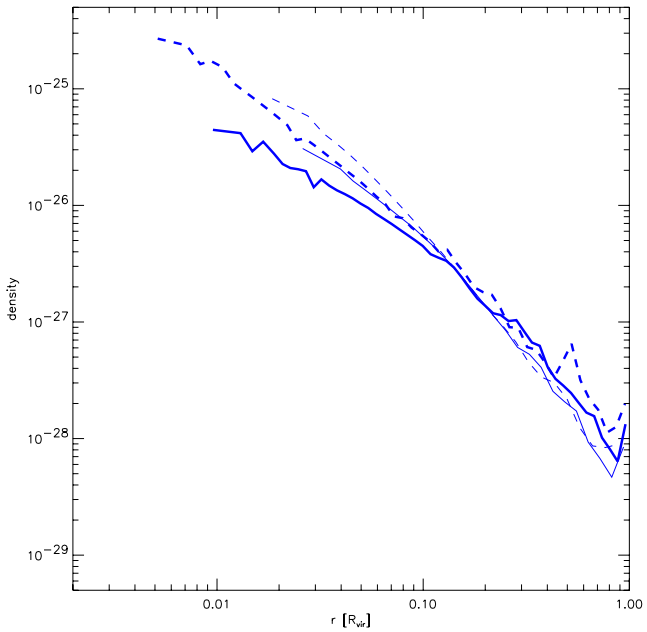

Figure 15. Radial gas density profile. The thick lines represent the average over the four massive clusters, whereas the thin lines give the average over the five low-mass systems. The dashed lines are drawn from the original viscosity simulations, and the solid lines from the low-viscosity simulations.

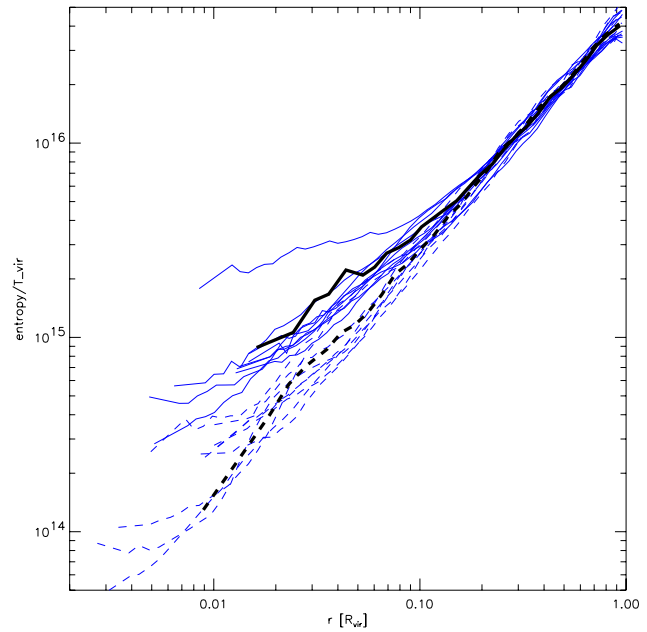

Figure 16. Radial entropy profiles of the ICM gas. Thin lines are individual profiles for the nine clusters, and thick lines are averages. The dashed lines are drawn from the original viscosity simulations, and the solid lines from the low-viscosity simulations.

In order to investigate a possible change of the accretion behaviour, we traced back to high redshift all particles that end up at $z = 0$ within 5 per cent of $R_{\rm vir}$ of the cluster centre. We find that most of the central material is located in the centres of progenitor haloes at higher redshift, which is a well-known result. However, in the simulations with the time-dependent, low-viscosity scheme, there is a clear increase of the number of particles which are not associated with the core of a halo at higher redshift. We illustrate this with the histograms shown in Fig. 17, which gives the distribution of the distance to the nearest halo in units of $R_{\rm vir}$ of the halo. All particles at distances larger than 1 are not associated with any halo at corresponding epoch. Compared to the low-entropy material that is already bound in a dense core at this epoch, this diffuse gas is brought to much higher entropy by shocks. When it is later accreted on to the cluster and mixed into the core, it can then raise the entropy level observed there. We note that Eulerian hydrodynamics simulations also show a flattening of the entropy profile. While the exact degree to which numerical and physical (turbulent) mixing contribute to producing this result is still a matter of debate, it is intriguing that a larger level of turbulence in the SPH calculations substantially alleviates the discrepancies in the results otherwise obtained with the two techniques (Frenk et al. 1999; O'Shea et al. 2005).

7 METAL LINES

Turbulent gas motions can lead to substantial Doppler broadening of X-ray metal lines, in excess of their intrinsic linewidths. Given the exquisite spectral resolution of the upcoming observational X-ray mission, this could be used to directly measure the degree of ICM turbulence (Sunyaev et al. 2003) by measuring, for example, the shape of the 6.702-keV iron emission line.

One potential difficulty in this is that multiple large-scale bulk motions of substructure moving inside the galaxy cluster along the line of sight might dominate the signal. To get a handle on this, we estimate the line-of-sight emission of the 6.702-keV iron line within columns through the simulated clusters, where the column size was chosen to be $300\,h^{-1}$ kpc on a side, which at the distance of the Coma cluster corresponds roughly to 1 arcmin, the formal resolution of *ASTRO-E2*. For simplicity, we assign every gas particle a constant iron abundance and an emissivity proportional to $n_{\rm e}^2 \times f(T_{\rm e}) \times \Delta V$, where $n_{\rm e}$ is the electron density and $\Delta V \propto \rho^{-1}$ is the volume represented by the particle. As a further approximation, we set the electron abundance equal to unity. We also neglect thermal broadening and other close lines (such as the 6.685-keV iron line), given that the 6.702-keV iron line is clearly the strongest.

In Fig. 18, we show the resulting distributions for several lines of sight, here distributed on a grid with -500, -250, 0, 250 and $500\,h^{-1}$ kpc impact parameter in the x-direction, and -250, 0 and 250, h^{-1} kpc impact parameter in the y-direction, respectively. The different lines in each panel correspond to simulations with the signal velocity based viscosity (dashed line) and with the time-dependent low-viscosity scheme (solid lines). Both results have been normalized to the total cluster luminosity, such that the integral under the curves corresponds to the fraction of the total luminosity.

We note that this measurement is very sensitive to small timing differences between different simulations, and therefore a comparison of the same cluster run with different viscosity should be carried out in a statistical fashion, even if some features look very similar in both runs. In general, we confirm previous findings (e.g. Inogamov & Sunyaev 2003) that large bulk motions can lead to spectral features which are several times wider than expected based on thermal broadening alone. Additional complexity is added by beam smearing effects, thermal broadening, and by the local turbulence in the ICM gas, such that an overall very complex line shape results. In our simulations with the low-viscosity scheme, where we have found an increased level of fluid turbulence, the final line shapes are indeed more washed out. However, the complexity of the final line shapes

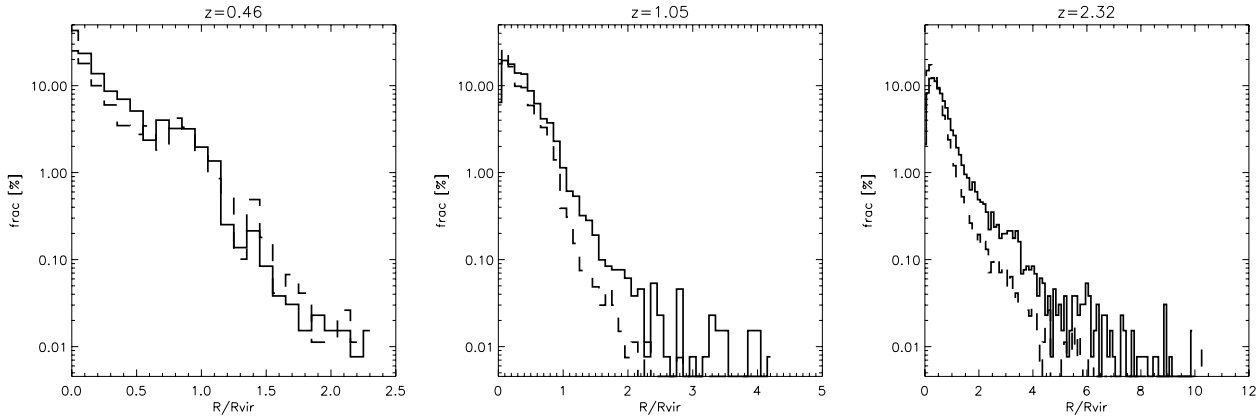

Figure 17. Distribution of the distance of particles to their nearest halo at high redshift. The particles selected here end up within 5 per cent of $R_{\rm vir}$ at $z = 0$. The dashed lines are for the original viscosity scheme, while the solid lines mark the result for the low-viscosity simulations.

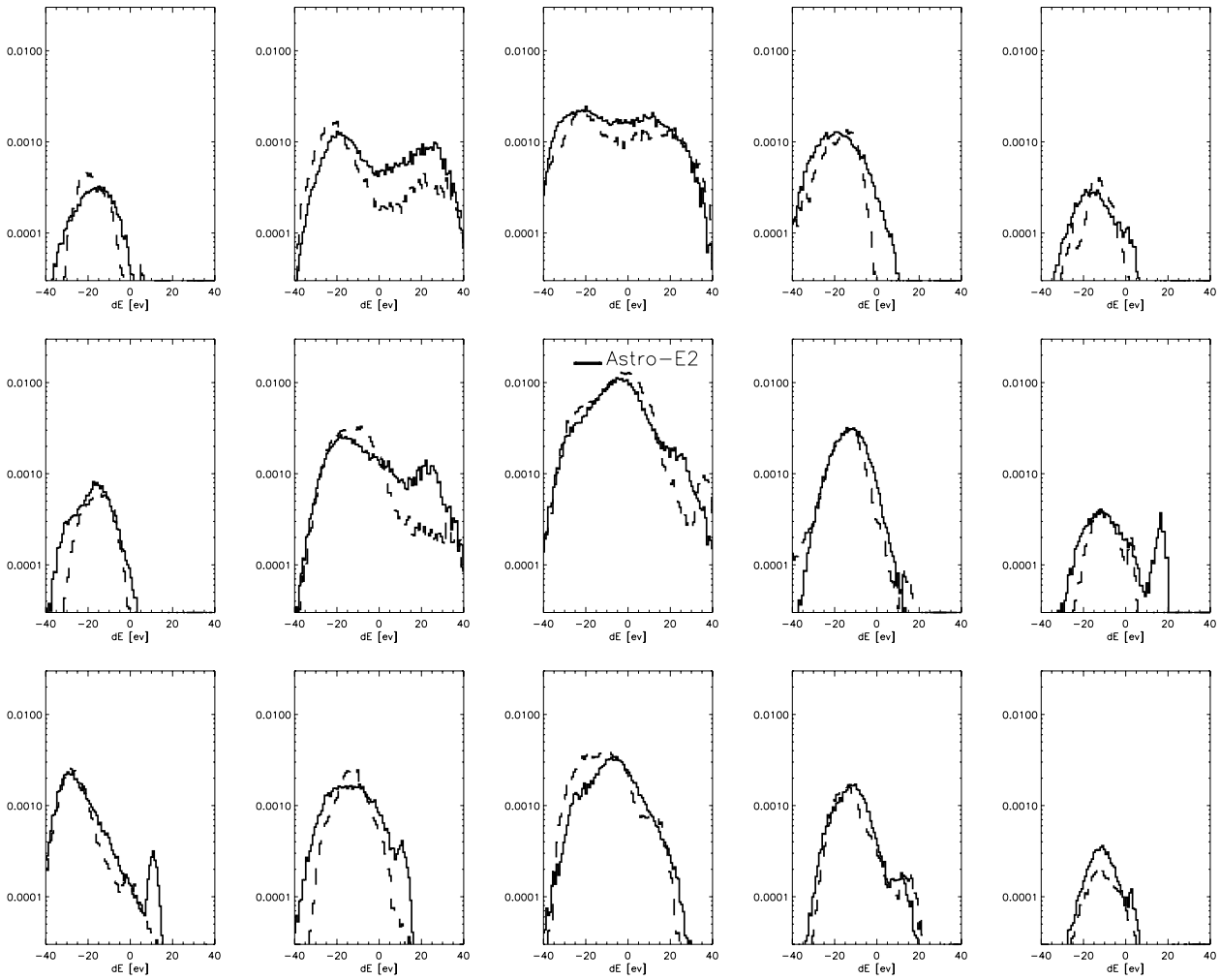

Figure 18. Distribution of the Doppler-shifted emission of the iron 6.702-keV line for 15 lines of sight through the cluster g72. Every panel corresponds to a column of side length $300\,h^{-1}$ kpc through the virial region of the cluster. This roughly corresponds to 1-arcmin resolution (comparable to the *ASTRO-E2* specifications) at the distance of the Coma cluster. The columns from left to right correspond to -500, -250, 0, 250 and $500\,h^{-1}$ kpc impact parameter in the x-direction, and the rows correspond to -250, 0 and 250, h^{-1} kpc impact parameter in the y-direction. The dashed lines give results for the original viscosity run, while the solid line is for the low-viscosity run. The thick bar in the centre panel marks the expected energy resolution of 12 eV as an indication for a high-resolution instrument with comparable specifications to the high-resolution X-ray Spectrometer (XRS) instrument on board *ASTRO-E2*.

suggests that it will be very difficult to accurately measure the level of fluid turbulence with high-resolution spectra of X-ray emission lines, primarily because of the confusing influence of large-scale bulk motions within galaxy clusters.

8 APPLICATION TO RADIO HALOES

One promising possibility to explain the extended radio emission on Mpc-scales observed in a growing number of galaxy clusters is to attribute it to electron acceleration by cluster turbulence (e.g. Schlickeiser, Sievers & Thiemann 1987; Brunetti et al. 2001). Having high-resolution cluster simulations at hand, which thanks to the new viscosity scheme are able to develop significant turbulence within the ICM, it is of interest to explore this possibility here. Obviously, due to the uncertainties in the complex physical processes of dissipation of the turbulent energy – which up to this point cannot be explicitly modelled in the simulations – our analysis is limited to a check whether or not turbulent re-acceleration can plausibly reproduce some of the main properties of radio haloes. In this scenario, the efficiency of electron acceleration depends on the energy density of MHD waves (Alfvén waves, fast mode waves, etc.), on their energy spectrum, and on the physical conditions in the ICM (i.e. density and temperature of the thermal plasma, strength of the magnetic field in the ICM, number density and spectrum of cosmic rays in the ICM). A number of approaches for studying the acceleration of relativistic electrons in the ICM have been successfully developed by focusing on the case of Alfvén waves (Ohno, Takizawa & Shibata 2002; Brunetti et al. 2004) and, more recently, on fast mode waves (Cassano & Brunetti 2005).

It should be stressed, however, that analytical and/or semi-analytical computations are limited to very simple assumptions for the generation of turbulence in the ICM. Full numerical simulations represent an ideal complementary tool for a more general analysis, where the injection of turbulence into the cluster volume by hierarchical merging processes can be studied realistically. Low numerical viscosity and high spatial resolution are however a prerequisite for reliable estimates of turbulence. As we have seen earlier, previous SPH simulations based on original viscosity parametrizations have suppressed random gas motions quite strongly, but the low-viscosity scheme explored here does substantially better in this respect.

In this section, we carry out a first exploratory analysis of the efficiency of electron acceleration derived in the low-viscosity scheme, and we compare it to results obtained with a original SPH formulation. For definiteness, we assume that a fraction η_t of the estimated energy content of the turbulent velocity fields in the cluster volume, measured by the local velocity dispersion (equation 16, Section 5), is in the form of fast mode waves. We focus on these modes since relativistic electrons are mainly accelerated by coupling with large-scale modes (e.g. $k^{-1} \geqslant$ kpc, k being the wavenumber) whose energy density, under the above assumption, can hopefully be constrained with the numerical simulations in a reliable fashion. In addition, the damping and time evolution of fast modes basically depend only on the properties of the thermal plasma and are essentially not sensitive to the presence of cosmic ray protons in the ICM (Cassano & Brunetti 2005).

Relativistic particles couple with fast modes via magnetic Landau damping. The necessary condition for Landau damping (Melrose 1968; Eilek 1979) is $\omega - k_{||} v_{||} = 0$, where ω is the frequency of the wave, $k_{||}$ is the wavenumber projected along the magnetic field, and $v_{||} = v\mu$ is the projected electron velocity. Note that in this case – in contrast to the Alfvénic case – particles may also interact with large-scale modes. In the collisionless regime, it can be shown that the resulting acceleration rate in an isotropic plasma (mode propagation and particle momenta) is given by (e.g. Cassano & Brunetti 2005)

$$\frac{\mathrm{d}p}{\mathrm{d}t} \sim 180\,\frac{v_{\rm M}^2}{c}\,\frac{p}{B^2}\int k\,W_k^B\,\mathrm{d}k, \tag{23}$$

where $v_{\rm M}$ is the magneto-sonic velocity, and W_k^B is the energy spectrum of the magnetic field fluctuations (e.g. Barnes & Scargle 1973; Cassano & Brunetti 2005). We estimate the rate of injection of fast modes, $I_k^{\rm FM}$, assuming that a fraction, η_t, of fluid turbulence is associated with these modes. We parametrize the injection rate assuming that turbulence is injected (and also dissipated) in galaxy clusters within a time of the order of a cluster-crossing time, $\tau_{\rm cross}$ (see Cassano & Brunetti 2005; Subramanian, Shukurov & Haugen 2005, for a more detailed discussion). We then have

$$\int I_k^{\rm FM}\,\mathrm{d}k \sim \eta_t\,\frac{E_t}{\tau_{\rm cross}} \sim \frac{1}{2}\,\eta_t \rho_{\rm gas}\sigma_v^2\,\tau_{\rm inject}^{-1}. \tag{24}$$

Here, $\tau_{\rm inject}$ is the time over which a merging substructure is able to inject turbulence in a given volume element in the main cluster. This can be estimated as the size of the subhalo divided by its infalling velocity. As the size of a halo is only a weak function of its mass, we approximate $\tau_{\rm inject}$ with a generic value of $\tau_{\rm inject} = 0.5$ Gyr. This is only a very crude estimate and more generally one should think of an effective efficiency parameter $\eta_t^{\rm eff} = \eta_t/\tau_{\rm inject}$ which we set to $0.1/(0.5\,\mathrm{Gyr})$ as argued before. Note also that for estimating σ_v^2 we used a 64^3 TSC grid, which is a conservative estimate, as shown in Fig. 4, and therefore equation (24) should still reflect a lower limit.

Following Cassano & Brunetti (2005), the spectrum of the magnetic fluctuations associated with fast modes is computed under stationary conditions taking into account the damping rate of these modes with thermal electrons, $\Gamma_k = \Gamma_o\,k$. We then have

$$W_k^B \sim \frac{B_o^2}{8\pi}\,\frac{1}{P_{\rm gas}}\,\frac{I_k^{\rm FM}}{\Gamma_o k}. \tag{25}$$

Thus the integral in equation (23) at each position of the grid can be readily estimated as

$$\int k\,W_k^B\,\mathrm{d}k \sim \frac{B_o^2}{8\pi}\,\frac{1}{\Gamma_o P_{\rm gas}}\int I_k^{\rm FM}\,\mathrm{d}k \tag{26}$$

$$\sim \eta_t^{\rm eff}\,\frac{B^2(\boldsymbol{x})}{16\pi}\,\frac{\rho_{\rm gas}(\boldsymbol{x})\sigma_{ii}^2(\boldsymbol{x})}{P_{\rm gas}(\boldsymbol{x})}\,\frac{1}{\Gamma_o} \tag{27}$$

where Γ_o depends on the temperature of the ICM (Cassano & Brunetti 2005).[1]

In this section we are primarily interested in determining the maximum energy of accelerated electrons, given the adopted energy density for fast modes. Under typical conditions in the ICM, the maximum energy of electrons is reached at energies where radiative losses balance the effect of the acceleration. The radiative synchrotron and inverse Compton losses with cosmic microwave background photons are given by (e.g. Sarazin 1999)

$$\left(\frac{\mathrm{d}p}{\mathrm{d}t}\right)_{\rm rad} = -4.8\times10^{-4}\,p^2\left[\left(\frac{B_{\mu G}}{3.2}\right)^2\frac{\sin^2\theta}{2/3} + (1+z)^4\right] = -\frac{\beta\,p^2}{m_{\rm e}\,c}, \tag{28}$$

where $B_{\mu\rm G}$ is the magnetic field strength in μG, and θ is the pitch angle of the emitting electrons. If an efficient isotropization of

[1] Note that under these assumptions the efficiency of the particle acceleration does not depend on the spectrum of the waves.

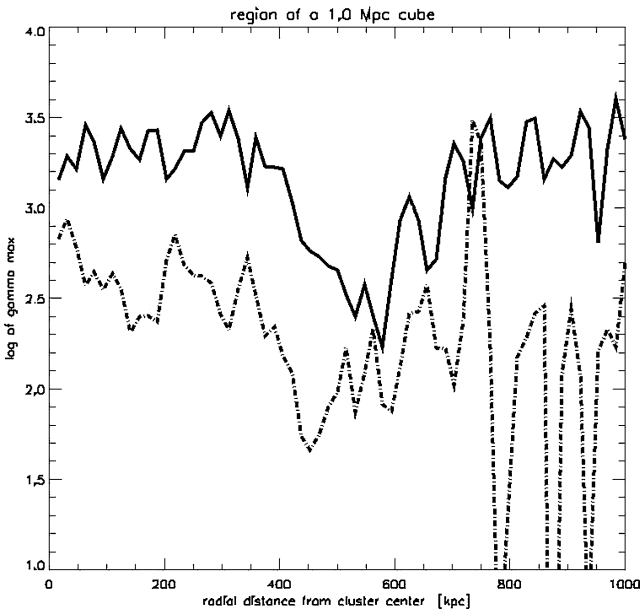

Figure 19. One-dimensional profile of the maximum energy of the electrons accelerated via the turbulent magneto-sonic model, along the same vertical lines drawn in Fig. 5. Dashed lines are for the original viscosity run, while solid lines are for the low-viscosity scheme. Here, a conservative 64^3 grid is used in the TSC smoothing.

electron momenta can be assumed, it is possible to average over all possible pitch angles, so that $\langle \sin^2 \theta \rangle = 2/3$.

In Fig. 19, we plot the maximum energy of the fast electrons obtained from equations (25) and (28) along one line of sight through the cluster atmosphere. The two different lines are for the same cluster, simulated with our two main schemes for the artificial viscosity. The two vertical lines in Fig. 5 are indicating the position of these cuts. When the new low-viscosity scheme is used, enough turbulence is resolved to maintain high-energy electrons (and thus synchrotron radio emission) almost everywhere out to a distance of 1 Mpc from the cluster centre, whereas in the original formulation of SPH, turbulence is much more strongly suppressed, so that the maximum energy of the accelerated electrons remains a factor of about 3 below that in the low-viscosity case.

The results reported in Fig. 19 are obtained assuming a reference value of $\eta_t^{\rm eff} = \eta_t/\tau_{\rm inject} = 0.1/(0.5\,{\rm Gyr})$. The averaged volume-weighted magnetic field strength in the considered cluster region is fixed at 0.5 μG and a simple scaling from magnetic flux-freezing, $B \propto \rho^{(2/3)}$, is adopted in the calculations, resulting in a central magnetic field strength of $B_0 = 5.0\,\mu$G. It is worth noting that the maximum energy of the accelerated electrons, $\gamma_{\rm max}$, scales with the energy density of the turbulence (and with the fraction of the energy of this turbulence channelled into fast modes η_t, equation 25). However the synchrotron frequency emitted by these electrons scales with the square of the turbulent energy ($\gamma^2_{\rm max}$). Interestingly, with the parameter values adopted in Fig. 19, a maximum synchrotron frequency of the order of $10^2(\eta_t/0.1)^2$ MHz is obtained in an Mpc-sized cluster region, which implies diffuse synchrotron radiation up to GHz frequencies if a slightly larger value of η_t is adopted.[2] On the other hand, we note that essentially no significant radio emission would be predicted if we had used the simulations with the original SPH viscosity scheme.

In real galaxy clusters, the level of turbulence which can form will also depend on the amount of physical viscosity present in the ICM gas (i.e. on its Reynolds number), which in turn depends on the magnetic field topology and gas temperature. It will presumably still take a while before the simulations achieve sufficient resolution that the numerical viscosity is lower than this physical viscosity. In addition, the details of the conversion process of large-scale velocity fields into MHD modes is still poorly understood and well beyond the capabilities of presently available cosmological simulations. However, our results here show that a suitable modification of the artificial viscosity parametrization within SPH can be of significant help in this respect, and it allows a first investigation of the role of turbulence for feeding non-thermal phenomena in galaxy clusters.

9 CONCLUSIONS

We have implemented a new parametrization of the artificial viscosity of SPH in the parallel cosmological simulation code GADGET-2. Following a suggestion by Morris & Monaghan (1997), this method amounts to an individual, time-dependent strength of the viscosity for each particle which increases in the vicinity of shocks and decays after passing through a shock. As a result, SPH should show much smaller numerical viscosity in regions away from strong shocks than original formulations. We applied this low-viscosity formulation of SPH to a number of test problems and to cosmological simulations of galaxy cluster formations, and we compared the results to those obtained with the original SPH formulation. Our main results can be summarized as follows.

(i) The low-viscosity variant of SPH is able to capture strong shocks just as well as the original formulation, and in some cases we even obtained improved results due to a reduced broadening of shock fronts. In spherical accretion shocks, we also obtained slightly better results due to a reduction of pre-shock entropy generation.

(ii) Using the low-viscosity scheme, simulated galaxy clusters developed significant levels of turbulent gas motions, driven by merger events and infall of substructure. We find that the kinetic energy associated with turbulent gas motion within the inner $\sim$1 Mpc of a $10^{15}\,h^{-1}\,{\rm M}_\odot$ galaxy cluster can be up to 30 per cent of the thermal energy content. This value can be still larger and reach up to 50 per cent in the very central part of massive clusters. In clusters with smaller masses ($\sim 10^{14}\,h^{-1}\,{\rm M}_\odot$) we find a smaller turbulent energy content, reaching only 5 per cent within the central Mpc. Within a comparable fraction of the virial radius, the corresponding fraction is however still of the order 10 per cent. These values are much larger than what is found when the original SPH viscosity is employed, which strongly suppresses turbulent gas motions.

(iii) The presence of such an amount of turbulence has an imprint on global properties of galaxy clusters, most notably reducing the bolometric X-ray luminosity in non-radiative simulations by a factor of $\approx$2. However, the global, mass-weighted temperature does not change.

(iv) The temperature profiles of galaxy clusters are only mildly changed by the presence of turbulence, but we observe a strong decrease of density within the central region of galaxy clusters, where the turbulence is providing a significant contribution to the total pressure. Also the radial entropy profiles show a significant flattening towards the cluster centre. This makes them more similar to the observed profiles based on X-ray observations. Note however

[2] Note that, for example, Cassano & Brunetti (2005) required $\eta_t \sim 0.2$–0.3 in order to reproduce the observed statistics of radio haloes.

that radiative cooling – which was not included in our simulations – can also modify the profiles substantially. We find that the higher entropy in the centre found in the low-viscosity simulations is largely a result of the more efficient transport and mixing of low-entropy in infalling material into the core of the cluster. We note that the elevated entropy levels found in our low-viscosity runs are more similar to the results found with Eulerian hydrodynamic codes than the original SPH ones.

(v) Turbulence in galaxy clusters broadens the shape of metal lines observable with high-resolution X-ray spectrographs having similar specifications as the X-ray Telescope on board *ASTRO-E2*. Depending on the strength of the turbulence and the dynamical state of the cluster, prominent features due to large-scale bulk motions may however become washed out and blended into a very complex line structure. In general, it will therefore be difficult to isolate the signature of the turbulent broadening and to differentiate it unambiguously from the more prominent features of large-scale bulk motions.

(vi) Applying a model for accelerating relativistic electrons by ICM turbulence we find that galaxy clusters simulated with the reduced viscosity scheme may develop sufficient turbulence to account for the radio emission that is observed in many galaxy clusters, provided that a non-negligible fraction of the turbulent energy in the real ICM is associated with fast modes.

In summary, our results suggest that ICM turbulence might be an important ingredient in the physics of galaxy clusters. If present at the levels inferred from our low-viscosity simulations, it has a significant effect on the radial structure and on the scaling relations of galaxy clusters. We also note that the inferred reduction of the X-ray luminosity has a direct influence on the strength of radiative cooling flows. Although simulations with reduced resolution are indicating that indeed the catastrophic cooling can be somewhat delayed by the presence of strong turbulence, too much gas still cools in the centre of galaxy clusters in the absence of feedback processes. However, a detailed analysis of simulations including radiative cooling is outside the scope of this paper. Such studies have to be devoted to future work, as it will be also necessary to deal with the supernova feedback, which by its self-regulating behaviour will add additional difficulties to extract the detailed role of the turbulence.

Compared to the predictions of numerical simulations (e.g. Tornatore et al. 2004), the metal content observed for large parts of the cluster interior seems to be more homogeneous. Here the more efficient mixing processes would also help to understand these differences between observations and numerical simulations. Finally, cluster turbulence may also play an important role for the dynamics of non-thermal processes in galaxy clusters.

Although we observe a rather high level of turbulence in the very centre of our simulated galaxy clusters when we use the low-viscosity scheme, it is likely that we are still missing turbulence due to the remaining numerical viscosity of our hydrodynamic scheme, and due to the resolution limitations, particularly in low-density regions, of our simulations. This problem should in principle become less and less severe as the resolution of the simulations is increased in future calculations. However, given that there is a some physical viscosity in real galaxy clusters which limits the Reynolds number of the ICM, it cannot be the goal to model the ICM as a pure ideal gas. Instead, future work should concentrate on accurately characterizing this physical viscosity of the ICM, which could then be directly incorporated into the simulations by means of the Navier–Stokes equations. Our results suggest that the low-viscosity formulation of SPH should be of significant help in reducing the numerical viscosity of SPH simulation below the level of this physical viscosity, and the present generation of simulations may already be close to this regime.

ACKNOWLEDGMENTS

Many thanks to Volker Springel for providing GADGET-2 and initial conditions for test problems. We acknowledge fruitful discussions with Stefano Borgani and want to thank Volker Springel and Torsten Ensslin for carefully reading and fruitful suggestions to improve the manuscript. The simulations were carried out on the IBM-SP4 machine at the 'Centro Interuniversitario del Nord-Est per il Calcolo Elettronico' (CINECA, Bologna), with CPU time assigned under an INAF-CINECA grant, on the IBM-SP3 at the Italian Centre of Excellence 'Science and Applications of Advanced Computational Paradigms', Padova and on the IBM-SP4 machine at the 'Rechenzentrum der Max-Planck-Gesellschaft' in Garching. KD acknowledges support by a Marie Curie Fellowship of the European Community programme 'Human Potential' under contract number MCFI-2001-01227. GB acknowledges partial support from MIUR through grant PRIN2004 and from INAF through grant D4/03/15.

REFERENCES

Balsara D. S., 1995, J. Comput. Phys., 121, 357
Barnes A., Scargle J. D., 1973, ApJ, 184, 251
Bertschinger E., 1985, ApJS, 58, 1
Brunetti G., 2003, in Bowyer S., Hwang C-Y., eds, ASP Conf. Ser. Vol. 301, Matter and Energy in Clusters of Galaxies. Astron. Soc. Pac., San Francisco, p. 349
Brunetti G., Setti G., Feretti L., Giovannini G., 2001, MNRAS, 320, 365
Brunetti G., Blasi P., Cassano R., Gabici S., 2004, MNRAS, 350, 1174
Buote D. A., 2001, ApJ, 553, L15
Cassano R., Brunetti G., 2005, MNRAS, 357, 1313
Choudhuri A. R., ed., 1998, The Physics of Fluids and Plasmas: An Introduction for Astrophysicists. Cambridge Univ. Press, New York
Dolag K., Bartelmann M., Lesch H., 1999, A&A, 348, 351
Dolag K., Bartelmann M., Lesch H., 2002, A&A, 387, 383
Eilek J. A., 1979, ApJ, 230, 373
Feretti L., 2002, in Pramesh Rao A., Swarup G., Gopal-Krishna, eds, Proc. IAU Symp. 199, The Universe at Low Radio Frequencies. Kluwer, Dordrecht, p. 133
Feretti L., Gioia I. M., Giovannini G., eds, 2002, Astrophysics and Space Science Library, Vol. 272, Merging Processes in Galaxy Clusters. Kluwer, Dordrecht
Frenk C. S. et al., 1999, ApJ, 525, 554
Fusco-Femiano R., Orlandini M., De Grandi S., Molendi S., Feretti L., Giovannini G., Bacchi M., Govoni F., 2003, A&A, 398, 441
Giovannini G., Tordi M., Feretti L., 1999, New Astron., 4, 141
Inogamov N. A., Sunyaev R. A., 2003, Astron. Lett., 29, 791
Mazzotta P., Rasia E., Moscardini L., Tormen G., 2004, MNRAS, 354, 10
Melrose D. B., 1968, AP&SS, 2, 171
Monaghan J. J., 1997, J. Comput. Phys., 136, 298
Monaghan J. J., Gingold R. A., 1983, J. Comput. Phys., 52, 374
Morris J. P., Monaghan J. J., 1997, J. Comput. Phys., 136, 41
Norman M. L., Bryan G. L., 1999, in Röser H.-J., Meisenheimer K., eds, Lect. Notes Phys. Vol. 530, The Radio Galaxy Messier 87. Springer, New York, p. 106
Ohno H., Takizawa M., Shibata S., 2002, ApJ, 577, 658
O'Shea B. W., Nagamine K., Springel V., Hernquist L., Norman M. L., 2005, ApJS, 160, 1
Poludnenko A. Y., Frank A., Blackman E. G., 2002, ApJ, 576, 832
Puchwein E., Bartelmann M., Dolag K., Meneghetti M., 2005, A&A, 442, 405

Ricker P. M., Sarazin C. L., 2001, ApJ, 561, 621
Roettiger K., Loken C., Burns J. O., 1997, ApJS, 109, 307
Roettiger K., Stone J. M., Burns J. O., 1999, ApJ, 518, 594
Sarazin C. L., 1999, ApJ, 520, 529
Schindler S., Mueller E., 1993, A&A, 272, 137
Schlickeiser R., Sievers A., Thiemann H., 1987, A&A, 182, 21
Schuecker P., Böhringer H., Reiprich T. H., Feretti L., 2001, A&A, 378, 408
Schuecker P., Finoguenov A., Miniati F., Böhringer H., Briel U. G., 2004, A&A, 426, 387
Sod G. A., 1978, J. Comput. Phys., 27, 1
Springel V., 2005, MNRAS, in press (astro-ph/0505010)
Springel V., Hernquist L., 2002, MNRAS, 333, 649
Springel V., Yoshida N., White S., 2001, New Astron., 6, 79
Steinmetz M., 1996, in Bender R., Davies R. L., eds, Proc. IAU Symp., 171, New Light on Galaxy Evolution. Kluwer, Dordrecht, p. 259
Subramanian K., Shukurov A., Haugen N. E. L., 2005, MNRAS, submitted (astro-ph/0505144)
Sunyaev R. A., Norman M. L., Bryan G. L., 2003, Astron. Lett., 29, 783
Takizawa M., 2005, ApJ, 629, 791
Tormen G., Bouchet F., White S., 1997, MNRAS, 286, 865
Tormen G., Moscardini L., Yoshida N., 2004, MNRAS, 350, 1397
Tornatore L., Borgani S., Matteucci F., Recchi S., Tozzi P., 2004, MNRAS, 349, L19
White S. D. M., Briel U. G., Henry J. P., 1993, MNRAS, 261, L8
Yoshida N., Sheth R., Diaferio A., 2001, MNRAS, 328, 669

This paper has been typeset from a TEX/LATEX file prepared by the author.